


Spring 2000

Kinetics of laser chemical vapor deposition of carbon and refractory metals

Feng Gao

Louisiana Tech University

Follow this and additional works at: <https://digitalcommons.latech.edu/dissertations>

 Part of the [Other Electrical and Computer Engineering Commons](#), [Other Materials Science and Engineering Commons](#), and the [Other Mechanical Engineering Commons](#)

Recommended Citation

Gao, Feng, "" (2000). *Dissertation*. 164.

<https://digitalcommons.latech.edu/dissertations/164>

This Dissertation is brought to you for free and open access by the Graduate School at Louisiana Tech Digital Commons. It has been accepted for inclusion in Doctoral Dissertations by an authorized administrator of Louisiana Tech Digital Commons. For more information, please contact digitalcommons@latech.edu.

INFORMATION TO USERS

This manuscript has been reproduced from the microfilm master. UMI films the text directly from the original or copy submitted. Thus, some thesis and dissertation copies are in typewriter face, while others may be from any type of computer printer.

The quality of this reproduction is dependent upon the quality of the copy submitted. Broken or indistinct print, colored or poor quality illustrations and photographs, print bleedthrough, substandard margins, and improper alignment can adversely affect reproduction.

In the unlikely event that the author did not send UMI a complete manuscript and there are missing pages, these will be noted. Also, if unauthorized copyright material had to be removed, a note will indicate the deletion.

Oversize materials (e.g., maps, drawings, charts) are reproduced by sectioning the original, beginning at the upper left-hand corner and continuing from left to right in equal sections with small overlaps.

Photographs included in the original manuscript have been reproduced xerographically in this copy. Higher quality 6" x 9" black and white photographic prints are available for any photographs or illustrations appearing in this copy for an additional charge. Contact UMI directly to order.

**Bell & Howell Information and Learning
300 North Zeeb Road, Ann Arbor, MI 48106-1346 USA
800-521-0600**

UMI[®]

**KINETICS OF LASER CHEMICAL VAPOR DEPOSITION OF
CARBON AND REFRACTORY METALS**

by

Feng Gao, B.S.

A Dissertation Presented in Partial Fulfillment
of the Requirements for the Degree
PH.D in Engineering

COLLEGE OF ENGINEERING AND SCIENCE
LOUISIANA TECH UNIVERSITY

November 2000

UMI Number: 9982759

UMI[®]

UMI Microform 9982759

Copyright 2000 by Bell & Howell Information and Learning Company.

All rights reserved. This microform edition is protected against
unauthorized copying under Title 17, United States Code.

Bell & Howell Information and Learning Company
300 North Zeeb Road
P.O. Box 1346
Ann Arbor, MI 48106-1346

LOUISIANA TECH UNIVERSITY

THE GRADUATE SCHOOL

October 05, 2000

Date

We hereby recommend that the thesis prepared under our supervision
by Feng Gao

entitled Kinetics of Laser Chemical Vapor Deposition of Carbon and Refractory metals

be accepted in partial fulfillment of the requirements for the Degree of
Ph.D in Engineering, Manufacturing System Engineering



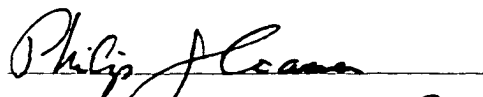
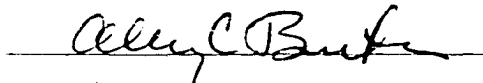
Supervisor of Thesis Research



Head of Department

Department

Recommendation concurred in:



Advisory Committee

Approved:



Director of Graduate Studies



Dean of the College

Approved:



Dean of the Graduate School

ABSTRACT

Three-dimensional laser chemical vapor deposition (3D-LCVD) has been used to grow rods of carbon, tungsten, titanium, and hafnium from a variety of hydrocarbons and metal halide-based precursors. A novel computerized 3D-LCVD system was designed and successfully used in the experiments. A focused Nd:Yag laser beam ($\lambda=1.06 \mu\text{m}$) was utilized to locally heat up a substrate to deposition temperature. The rods, which grew along the axis of the laser beam, had a typical diameter of 30 – 80 μm and a length of about 1 mm. The precursors for carbon deposition were the alkynes: propyne, butyne, pentyne, hexyne, and octyne. Propyne gave the highest deposition rate, in excess 3 mm/s at high laser powers (0.45 W) and high partial pressures (3000 mbar). The temperature dependence and pressure dependence were both non-linear functions of the growth rate. The temperature dependence could be separated into two regions – the kinetically limited region, which obeys the Arrhenius relationship, and the transport limited region, which is explained by diffusion of the precursors to the reaction zone. The pressure dependence showed that the reaction order for the different precursors varied from 2.5 for propyne to 1.3 for octyne.

The precursors used to deposit the refractory metals were tungsten hexafluoride, titanium tetraiodide and hafnium chloride. The only successful precursor was tungsten hexafluoride, which readily produced tungsten rods when mixed with hydrogen. Rod diameters typically ranged from 50 μm to 400 μm and the average length of the rods

were about 1 mm. Much lower deposition rates, less than $4.5 \mu\text{m/s}$, were obtained in this case as compared to carbon deposition. By an optimization of the LCVD process, it was possible to deposit high-quality single crystal tungsten rods. They were all oriented in the $\langle 100 \rangle$ direction.

APPROVAL FOR SCHOLARLY DISSEMINATION

The author grants to the Prescott Memorial Library of Louisiana Tech University the right to reproduce, by appropriate methods, upon request, any or all portions of this Thesis. It is understood that "proper request" consists of the agreement, on the part of the requesting party, that said reproduction is for his personal use and that subsequent reproduction will not occur without written approval of the author of this Thesis. Further, any portions of the Thesis used in books, papers, and other works must be appropriately referenced to this Thesis.

Finally, the author of this Thesis reserves the right to publish freely, in the literature, at any time, any or all portions of this Thesis.

Author Feng Gao

Date 10/10/2000

TABLE OF CONTENTS

	Page
ABSTRACT	iii
LIST OF TABLES	viii
LIST OF FIGURES	ix
ACKNOWLEDGMENTS	xi
CHAPTER	
1. INTRODUCTION	01
1.1 Rapid Prototyping.....	02
1.2 MEMS Applications.....	04
1.3 Thin Film Deposition.....	07
1.4 Laser Chemical Vapor Deposition (LCVD).....	10
1.5 Research Needs and Objectives of This Dissertation.....	11
1.6 Organization of This Dissertation.....	12
2. THEORY OF LASER CHEMICAL VAPOR DEPOSITION	14
2.1 LCVD Mechanisms.....	14
2.1.1 Photolytic LCVD.....	14
2.1.2 Thermal LCVD.....	16
2.2 LCVD Deposition Rate Limited.....	18

2.2.1 Kinetically-Limited Regime.....	20
2.2.2 Transport-Limited Regime.....	20
2.2.3 Thermodynamic-Limited Regime.....	21
2.3 LCVD Process Parameters.....	22
3. LITERATURE REVIEW.....	28
3.1 Two-Dimensional LCVD.....	30
3.2 Three-Dimensional LCVD.....	37
4. EXPERIMENTAL SETUP AND EXPERIMENTAL PROCEDURE.....	43
4.1 Experimental Setup.....	43
4.2 Experimental Procedure.....	56
5. RESULTS AND DISCUSSIONS.....	60
5.1 Deposition of Carbon from Alkynes.....	60
5.1.1 Growth Rate as a Function of Laser Power.....	60
5.1.2 Growth Rate as a Function of Pressure.....	66
5.1.3 Rod Diameter as a Function of Laser Power.....	71
5.1.4 Rod Diameter as a Function of Pressure.....	74
5.2 Deposition of Tungsten.....	80
5.3 Deposition of Titanium and Hafnium.....	82
6. CONCLUSIONS AND FUTURE WORK.....	85
REFERENCES.....	88

LIST OF TABLES

Table	Page
1.1 Ten steps of photolithgraphy process ^[7]	05
1.2 CVD reaction mechanisms.....	08
1.3 Different CVD processes ^[8]	09
1.4 Methods of laser processing ^[9]	10
2.1 Classification of process parameters in LCVD	23
5.1 Growth rate range for each alkyne in constant pressure experiments.....	70
5.2 Rod diameter range for constant laser power experiments.....	76

LIST OF FIGURES

Figure	Page
1.1 3D-LCVD as a MEMS prototyping tool ^[2]	01
2.1 Photolytic processing.....	15
2.2 Thermal processing ^[10]	17
2.3 Growth rates.....	18
2.4 Rate-limited regimes.....	19
3.1 Direct writing using 2D-LCVD.....	29
3.2 Fiber growth using 3D-LCVD.....	29
3.3 Trussed carbon structure ^[35]	39
3.4 Taped carbon rods ^[37]	40
3.5 Diamond-like carbon microcoil ^[37]	40
3.6 Single crystal tungsten rod ^[37]	41
3.7 Tungsten on boron microsolenoid by laser direct-writing ^[37]	42
4.1 3D-LCVD subsystems.....	44
4.2 Schematic diagram of the 3D-LCVD setup.....	45
4.3 LCVD reactor.....	46
4.4 Reaction system – substrate holder.....	48
4.5 Reaction system – aluminum chamber.....	49
4.6 PID control flowchart.....	51
4.7 Vacuum system – mechanical pump.....	52

4.8	Vacuum system – helium leak detector.....	53
4.9	Gas-handling system – precursor cylinder.....	54
4.10	Imaging system.....	55
4.11	Frontview of the whole LCVD systems.....	55
4.12	An example of carbon rods grown on silicon substrate.....	58
4.13	SEM – ARMAY 1830.....	59
5.1	Growth rate as a function of laser power for alkynes.....	61
5.2	Curve-fit for exponential region – alkynes.....	62
5.3	Curve-fit for linear region – alkynes	64
5.4	Smooth amorphous rods – low powers.....	65
5.5	Polycrystalline (small-grains) rods – middle power.....	66
5.6	Growth rate as a function of partial pressure for alkynes-linear.....	67
5.7	Growth rate as a function of partial pressure for alkynes-logarithm.....	68
5.8	Rod of constant diameter with smooth surface.....	71
5.9	Rod diameter as a function of laser power for alkynes	72
5.10	Relationship between temperature distribution and rod diameter.....	74
5.11	Relationship between activation energy and rod diameter.....	74
5.12	Rod diameter as a function of partial pressure for alkynes.....	76
5.13	Volumetric growth rate as a function of partial pressure for alkynes-linear.....	78
5.14	Volumetric growth rate as a function of partial pressure for alkynes-logarithm...79	
5.15	Growth rate as a function of laser power for tungsten deposition.....	81
5.16	Rods in different morphologies.....	81
5.17	Rod diameter as a function of laser power for tungsten deposition.....	82

ACKNOWLEDGMENTS

I would like to express my sincere gratitude to my advisor, Dr. Mats Boman, and former advisor, Dr. James Maxwell, for their advice, continuous guidance, and encouragement – all necessary for completion of this dissertation. I also appreciate the time and support of my advisory committee: Dr. Meng Tao, Dr. Tianhong Cui, Dr. Alley Butler, and Mr. Philip Coane.

I dedicate this dissertation to my wife and my daughter whose love, patience, and encouragement accompanied me through this research.

CHAPTER 1

INTRODUCTION

At the forefront of current manufacturing technology are three major topics of research, namely Rapid Prototyping techniques, Micro-Electro-Mechanical Systems (MEMS) based application, and microelectronics based thin film deposition techniques. Researchers worldwide, as shown in Figure 1.1, are investigating these techniques. As an intersection of these three areas, three-dimensional laser chemical vapor deposition (3D-LCVD^[1]) has emerged as a new rapid prototype technique for micro-scale components for MEMS based application. The following sections will briefly discuss these three areas.

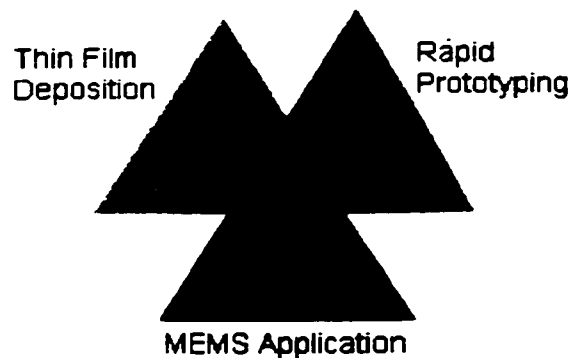


Figure 1.1 3D-LCVD as a MEMS prototyping tool.^[2]

1.1 Rapid Prototyping

Rapid prototyping is also known as solid freeform fabrication (SFF). This technique offers several advantages over conventional manufacturing technologies. First, SFF can fabricate both large and/or small objects, which is especially important in micro-mechanical manufacturing. Second, rapid prototyping of the manufactured part allows for iterative fine-tuning of the design after which the part can be used or tested immediately. Parts produced by SFF can be used not only for making better prototypes, but also for low yield production in emerging “mass customization” markets. Third, SFF processes can be used to fabricate complex structures that can not be realized with traditional fabrication methods. SFF processes generally consist of three components: (1) an electronic representation of the prototype in three-dimension in a computer, (2) a driver which converts the representation to machining instructions, and (3) a process that can manufacture three-dimensional solid objects from designs with a minimum of constraints. In short, rapid prototyping is developed to shorten the development cycle significantly. The most successfully developed rapid prototyping techniques are microstereolithography, selectively laser sintering, and laminated object manufacturing.

Microstereolithography is a new process that allows manufacturing of small 3D complex objects. In contrast to planar microfabrication processes based on silicon micromachining, which evolved from the microelectronics technologies, microstereolithography processes find their origin in the rapid prototyping industry. As in the stereolithography process, all microstereolithography processes are based on a layer-by-layer light induced polymerization of a liquid resin. Microstereolithography processes developed until now are based on a vector-by-vector tracing of each layer obtained by

moving a focused light beam on the surface of a photopolymerizable liquid. More recently, Beluze *et al.*^[4] described a new microstereolithography process in which a complete layer can be built using a single exposure. Objects with complex shape from a computer aid design (CAD) program can be manufactured with microstereolithography process, such as micro-turbine and micro-cups. Its applications are focused on microfluidics, microrobotics, packaging or biomedical domains.

As a derivative application of microstereolithography, laser induced polymerization^[5] (LIP) has shown great advantages and is a fast growing area where electronic and mechanical components are combined to form miniature structures. In LIP, a focused laser is guided directly to write three-dimensional patterns. The advantages are high cure speed, constant intensity along the curing distance, and uniform exposure over the curing area. These advantages will result in more efficient absorption by selecting an appropriate photoinitiator and reducing the unwanted reactions which are common in conventional UV light curing. These advantages also lead to a more precise control of the penetration profile.

Selectively laser sintering (SLS) is a thermal process using a laser to sinter layers of powdered thermoplastic materials together to form solid 3D objects. SLS uses a flat sheet of powder heated to near its melting point. Then the laser beam scans over the powder and further heats the grains locally so that they melt on the outside and stick together. The base plate moves down slightly, and the next layer of powder is spread across the surface by a rotation roller. At the end of the build process, the entire cake of powder, sintered and unsintered, is allowed to cool and is lifted out of the machine. Then the loose powder is shaken off in order to free the sintered object. The advantage of SLS

is that numerous plastic materials can be used; one disadvantage is that toxic gases emitted from the fusing process have to be handled carefully.

Laminated object manufacturing^[6] (LOM) is a process commonly used to fabricate components that cannot be readily fabricated by conventional forming techniques, such as machining, casting, and modeling. Complex shapes, internal cavities, flow chambers, and interconnects can be achieved by LOM techniques. The lamination process is based on geometrical data. The starting point is the sliced data of the object used for controlling a laser beam that cuts the contours of thin sheets of materials. During the process, these sheets are glued together, and the desired model is created layer by layer. A variety of organic and inorganic materials, such as paper, plastic, or composites, can be used in this process. Parts produced by this process are virtually stress-free. Also, the cost of the process is low, and the processing time is short. The disadvantage of this process is that the stability of the objects produced is limited by the bonding strength of the glued layer. Moreover, hollow parts like bottles and small cylinders cannot be built by this method.

1.2 MEMS Applications

MEMS deals with systems wherein different micro-components are assembled together to make a microdevice. Each component contributes either electrically, mechanically, or chemically to give a fully functional device such as pressure transducers, accelerometers, micro-turbine, and chemical sensors, etc. In short, MEMS refers to a broad class of micro-machined sensors, actuators, and systems that exploit thermal, electrical, mechanical, optical, magnetic, acoustic, and chemical phenomena.

High aspect ratio microstructures (HARM) are a general requirement of these microsystems. Some of the HARM processes developed for MEMS in the past have included photolithography, X-ray lithography (LIGA), electron-beam lithography, ion-beam lithography, and focused ion beam (FIB).

The most widely used form of lithography is photolithography, by which a pattern is transferred from a mask onto a thin film. This process can be simply described by the ten-step process,^[7] listed in Table 1.1. The key parameter of this process is the critical dimension (CD) or the lateral resolution. Recently, CD of 0.1 μm or below has been achieved with phase-shifting masks (PSM) under DUV light exposure.

Table 1.1 Ten steps of photolithography process.^[7]

Step	Process description	Purpose
1	Surface preparation	Clean and dry wafer surface
2	Apply photoresist	Spin coat a thin layer of photoresist on surface
3	Softbake	Partial evaporation of photoresist solvent by heating
4	Alignment and exposure	Precise alignment of mask to wafer and exposure
5	Development	Removal of unpolymized resist (negative resist)
6	Hardbake	Additional evaporation of solvents
7	Develop inspect	Inspect surface for alignment and defects
8	Etch	Top layer of wafer is removed
9	Photoresist removal	Remove photoresist layer from wafer
10	Final inspection	Surface inspection for etch irregularities and others

The main advantage of photolithography is that it is suitable for batch processing, so a low production cost can be expected from this process. On the other hand, although photolithography can achieve submicron feature size with relatively low cost, it is not useful for fabricating high aspect ratio microstructures because of several limiting factors, such as optical sensitivity, contrast, and depth of focus (DOF).

These limitations are partially overcome in X-ray lithography (LIGA). LIGA involves a thick layer of X-ray resist, such as PMMA, from microns to centimeters, a high-energy X-ray radiation exposure and development. The result is a 3D-resist structure. Subsequent electro-deposition fills the resist mold with a metal, and after resist removal, a free standing metal structure results. LIGA's main advantages over photolithography rely on that it can produce high aspect ratio microstructure due to its very large DOF, higher resolution due to shorter wavelength used, and its high reproducibility. The drawback of LIGA is that this process is extremely expensive due to the need of X-ray synchrotron radiation and the fact that it cannot fabricate 3D microstructures with curved surfaces.

The electron beam (E-beam) lithography^[8] method, like X-ray lithography, has a high theoretic resolution because the wavelength of high energy electrons are very small. Two major advantages of electron beam lithography are:

- 1) The ability to register accurately over small areas of a wafer, lower defect densities, and a large depth of focus because of the short wavelength.
- 2) It can build the microstructures directly without the use of mask, i.e., it is a direct write type of microfabrication method which can be either additive or subtractive.

Some disadvantages of E-beam lithography are:

- 1) Electrons scatter quickly in solids, which limits the practical resolution.
- 2) Electrons, being charged particles, need vacuum, making the apparatus more complex than for photolithography.
- 3) Relatively slow exposure speed is because of a direct writing method. Due to these disadvantages, the use of E-beam lithography has been limited to mask-making and wafer-making, except for some specialized applications.

1.3 Thin Film Deposition

Thin film deposition as an additive pattern transfer technique stands out as an inevitable process in both microelectronics and MEMS fabrication. It can be categorized into two major types, namely, physical vapor deposition (PVD) and chemical vapor deposition (CVD).

Thermal evaporation and sputtering are two examples of physical vapor deposition. Thermal evaporation, one of the oldest thin film deposition techniques, is based on the evaporation of a heated material onto a substrate in high vacuum. A metal filament is usually evaporated by passing a high current through a refractory containment structure. This method is called resistive heating. However, electron-beam and radio frequency (RF) induction evaporation have surpassed resistive heating and are widely used for industrial applications.

Sputtering is preferred over evaporation in many applications due to a wider choice of materials to work with, better step coverage, and better adhesion of the film to the substrate. During sputtering, the target, which is held at a high negative potential, is bombarded with positive argon ions created in a plasma or glow discharge. The target

material is sputtered away mainly as neutral atoms by momentum transfer, and ejected surface atoms are deposited onto the substrate placed close to the anode. The most negative aspects in sputtering are the complexity of the process compared to an evaporation process, the excessive substrate heating due to secondary electron bombardment, and a relatively slow deposition rate.

The CVD method is a very versatile method and works in a broad pressure range at relatively high temperatures. Amorphous, polycrystalline, epitaxial, and uniaxially-oriented polycrystalline layers can be deposited with a high degree of purity, control, and economy. During chemical vapor deposition (CVD), the constituents or precursors of a vapor phase, often diluted with an inert carrier gas, react on a hot surface to deposit a solid film. The various steps are summarized in Table 1.2. CVD is a large family of coating technologies, such as atmosphere pressure CVD (APCVD), low pressure CVD (LPCVD), plasma-enhanced CVD (PECVD), and metal-organic CVD (MOCVD). The advantages, disadvantages, and applications of these kinds of CVD are summarized in Table 1.2.

Table 1.2 CVD reaction mechanisms.

- Mass transport of reactant and diluent gases in the bulk gas flow region from the reactor inlet to the deposition zone.
- Gas-phase reactions (homogenous) leading to film precursors and by-products.
- Mass transport of film precursors and reactants to the growth surface.
- Adsorption of film precursors and reactants on growth surface.
- Surface reactions (heterogeneous) of adatoms occurring selectively on the heated surface.

Table 1.2 CVD reaction mechanisms. (Continued)

Table 1.3 Different CVD processes.^[8]

Process	Advantages	Disadvantages	Applications
APCVD	Simple, high deposition rate, low temperature	Poor step coverage, particle contamination	Doped and undoped low temperature oxide
LPCVD	Excellent purity and uniformity, conformable step coverage, large wafer capacity	High temperature and low deposition rate	Doped and undoped high temperature oxide, silicon nitride, polysilicon, tungsten, etc.
PECVD	Fast, low substrate temperature, good adhesion and step coverage, low pinhole density	Chemical and particulate contamination	Low temperature insulators over metals, passivation (nitride)

Table 1.3 Different CVD processes.^[8] (Continued)

MOCVD	Excellent for epitaxy on large surface areas	Safety concerns	Compound semiconductors for solar cells, laser, photocathodes, LEDs, etc.
-------	--	-----------------	---

1.4 Laser Chemical Vapor Deposition (LCVD)

Laser induced processing has been widely exploited in the microelectronics and MEMS areas to produce deposits with well controlled chemical composition, feature size, and morphology. Laser processing methods can be divided into gas phase processing or liquid laser processing, which are listed in Table 1.4.

Table 1.4 Methods of laser processing.^[9]

Reactant phase	Method of excitation	Process
Gas	Thermal,	Localized (LCVD).
	Photochemical.	Photochemically-assisted CVD, localized.
Liquid	Thermal-	Laser assisted electroplating.
	electrochemical,	Laser assisted electroless plating.
		Thermal battery electroplating.
	Photo-	Electroplating.
	electrochemical	Electroless plating.

Photochemical LCVD implies a photochemical activation in the gas phase which results in the formation of reactive species or atoms that are then transported to the substrate and the growing film or the solids formed homogeneously in the gas phase. The thermal process is analogous to large area chemical vapor deposition, with the important exception that the reaction zone is localized. Thermal reactions take place on the surface in the region heated by the laser light. One of the primary applications of thermal LCVD is the direct writing of micron-sized spots and lines of a material onto a surface. Processes that make use of LCVD include the customization and repair of integrated circuit repair, electronic packaging, and lithographic masks. Other applications include depositing high purity metals at relative fast growth rates, such as nickel, copper, aluminum, zinc, gold, platinum. In all these applications, the requirement of high deposition rate is one of the primary goals.

1.5 Research Needs and Objectives of This Dissertation

While much progress has been made in recent years in microfabrication techniques, there remains fundamental constraint in the manufacture of MEMS via conventional means. It is desirable to have a process that would allow rapid prototyping on the micro-scale effectively, accurately, and quickly.

Bulk and surface micromachining have been the primary means of fabricating micromechanical devices over the last decade. Both of these processes employ photolithography and selective chemical etching to obtain the desired microstructure. However, conventional lithography for fabricating these microstructures is limited to unidirectional extensions of 2D patterns. Only simple 3D structures are possible, which

hardly meet the requirements of MEMS applications. Today, truer 3D structures are required to optimize structural characteristics, such as mechanical function, strength, flow properties, fracture resistance.

As an intersection between RP and thin film deposition, the LCVD technique provides a unique way of modifying the substrate surface or building the microstructure by depositing the material with desired mechanical, electrical, and optical properties. By using highly localized laser induced chemical reactions and accurate scanning of the laser beam, a wide range of MEMS devices can be fabricated at fast rates. This research aims at establishing the viability of using 3D-LCVD as a fast, low cost, and versatile tool to generate MEMS devices.

In detail, the goals of this thesis are (1) Design an effective high-pressure and high-temperature LCVD system for microscale fabrication of full 3D parts starting with the simplest shapes such as rods; (2) Demonstrate very rapid, convectively-enhanced growth; (3) Test a variety of precursors without making changes to the system; and (4) Study the effect of process parameters like laser power and precursor partial pressure on the deposition rates and diameters of rods.

1.6 Organization of This Dissertation

This dissertation mainly investigates 3D-LCVD as a viable rapid-prototyping tool. A number of experiments were performed by varying parameters such as laser power and partial pressure.

Chapter 1, as an introduction, describes the relationship among rapid prototyping, MEMS application, and thin film deposition. Background of LCVD is also provided here.

Chapter 2 gives a review for 2D-LCVD and 3D-LCVD, where growth of different types of thin film and microstructures are reviewed. Chapter 3 provides the necessary technical background for LCVD. Chapter 4 presents experimental apparatus and the method of experimentation in detail. Chapter 5 discusses experimental results for carbon, tungsten, titanium, and hafnium. Chapter 6 summarizes the conclusions and identifies future work.

CHAPTER 2

THEORY OF LASER CHEMICAL VAPOR DEPOSITION

2.1 LCVD Mechanisms

Laser chemical vapor deposition is a technique for depositing thin films of various materials on a substrate by inducing chemical reactions using a laser beam. LCVD is carried out through two possible mechanisms: photolytic dissociation of precursor or thermal dissociation of the precursor, or a combination of both processes.

2.1.1 Photolytic LCVD

Photolytic LCVD relies on the interactions of the laser beam with the chemical reactants. The precursor molecules absorb the photons of the laser beam, which in the visible UV-region cause the chemical bonds to break leading to the formation of highly reactive species. These species react in the gas phase and/or on the substrate surface where they form the deposit. Usually, visible and ultraviolet (UV) lasers are used for photolytic LCVD because the photon energy is comparable to, or exceeds, the chemical bond energy of many chemical compounds. The laser and precursors in photolytic LCVD are chosen so that (1) the precursor molecules have a large absorption cross-section for the laser beam; and (2) the chemical bond energy of the precursor molecules is less than

or equal to the energy of a photon of the laser beam. Both single and multi-photon excitations may be required to drive photolytic dissociation reactions, depending on the precursors used. A typical photolytic process is shown in Figure 2.1.

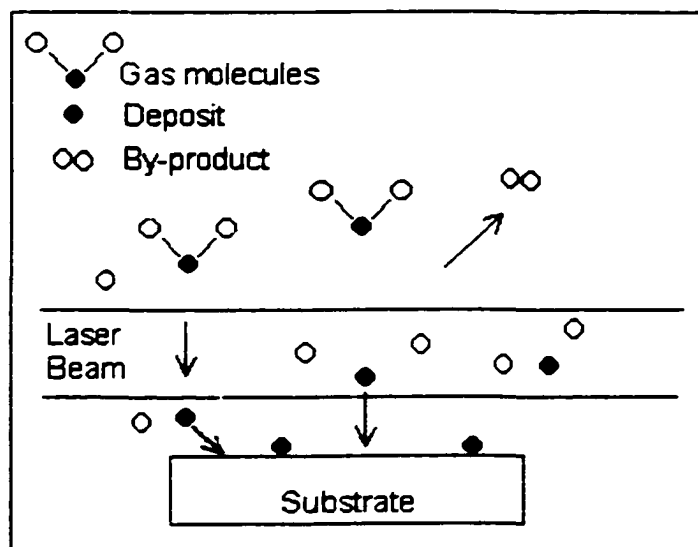


Figure 2.1 Photolytic processing.

In photolytic LCVD, photolysis of a precursor gas is generally carried out in either a parallel or orientation of the beam relative to the substrate.

The parallel configuration is employed to grow blanket deposits across a wafer and is often called photo-assisted CVD. In photo-assisted CVD processes, chemical reactions take place in the gas or vapor phase resulting in the formation of highly reactive intermediate species. This process usually means that the deposition temperature can be lowered. This lower deposition temperature is an attractive feature for the fabrication of semiconductors or other semiconductor devices because thermally-induced residual stress and impurity redistribution are minimized at lower temperature.

The direct-write photolysis is a photo-assisted CVD, except that the beam is at least partially focused onto the substrate. Deposition occurs only near the focus of the beam where the dissociated radicals diffuse to the deposit surface from the gas phase, and/or adsorbed precursor molecules are dissociated on the substrate surface. The direct writing method is useful for small-scale integrated (LSI) fabrication, mask and wafer repair. However, the writing rate is slow, approximately from 1 Å/min to 1 μm/sec.

2.1.2 Thermal LCVD

In thermal LCVD, on the other hand, the laser beam interacts mainly with the substrate to produce a hot spot where thermally-assisted chemical reactions take place resulting in the final product. The reactants, that is, precursors for thermal LCVD, must be selected in such a way that the chemical reactions can occur at a temperature below the melting temperature of the substrate. The gas phase should be transparent to incident laser light to avoid absorption of the light. Usually infrared lasers, such as Nd:YAG and CO₂ lasers, are used for thermal LCVD. A typical thermal process is shown in Figure 2.2

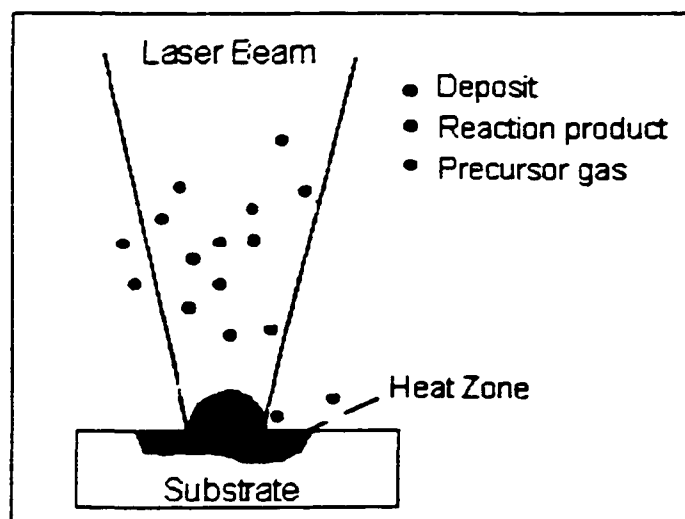


Figure 2.2 Thermal processing.^[10]

In this process, the laser is used to activate the gas phase precursors non-thermally. The laser beam can also activate the substrate non-thermally, i.e., band gap excitation. This activation can be transferred to adsorbed species on the substrate with subsequent non-thermal chemical reactions.

In case of direct heating, see Figure 2.2, the reactants, which can be a gas, liquid, or solid phase, are chosen in such a way that the substrate absorb the laser energy. When the temperature of the locally heated substrate surface reaches the reaction threshold temperature, the chemical reactions will occur.

Compared to photolytic deposition, thermal deposition generally occurs at much higher rates (often by several orders of magnitude). Typical deposition rates are from 0.1 $\mu\text{m}/\text{sec}$ to several millimeters per second. The main advantage of thermal deposition is the higher lateral resolution than its photolytic counterpart.

2.2 LCVD Deposition Rate Limited

For a typical 3D-LCVD process, three types of growth rates can be defined: the normal or local deposition growth rate, the axial or linear growth rate, and the volumetric or mass growth rate. All are shown in Figure 2.3. The normal growth rate (R_n) is defined as the growth rate measured normal to any point on the surface. The axial deposition rate (R_a) is a measure of the maximum growth rate at the center of the beam and along the x-axis (parallel to the laser beam). The axial growth rate is a good measure of the reactivity of a precursor used. The volumetric growth rate (R_v) is the growth rate of the overall three-dimensional volume of the deposit. Determination of the volumetric deposition rate is of utmost importance in evaluating the feasibility of any process for MEMS manufacture. For useful three-dimensional structures to be created at reasonable speeds, volumetric deposition rates on the order of 10^4 - $10^5 \mu\text{m}^3/\text{sec}$ or greater must be reached.

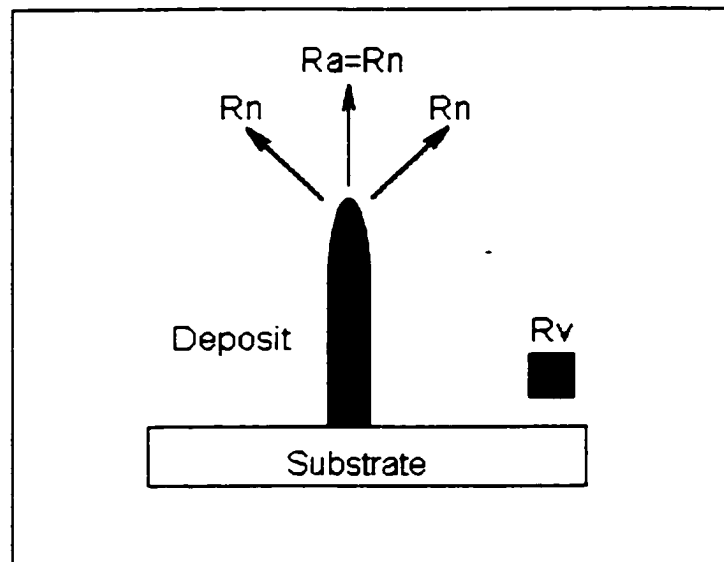


Figure 2.3 Growth rates.

In the following sections, the factors, which limit the deposition rate, will be discussed together with the fundamental relations that describe pyrolytic LCVD kinetics.

Although the deposition rate of a heterogeneous thermal reaction is driven by the surface temperature, the rate obtained depends on the reaction activation energy and the ability of the reactants and products to be transported to and from the surface. Generally, there are three types of rate-limited regimes, namely, kinetically limited regime, thermodynamically limited regime, and mass-transport limited regime. The relationship between these rate-limited regimes and temperature is shown in Figure 2.4. The actual deposition rate is determined by the slowest of these constraints for a given set of process parameters.

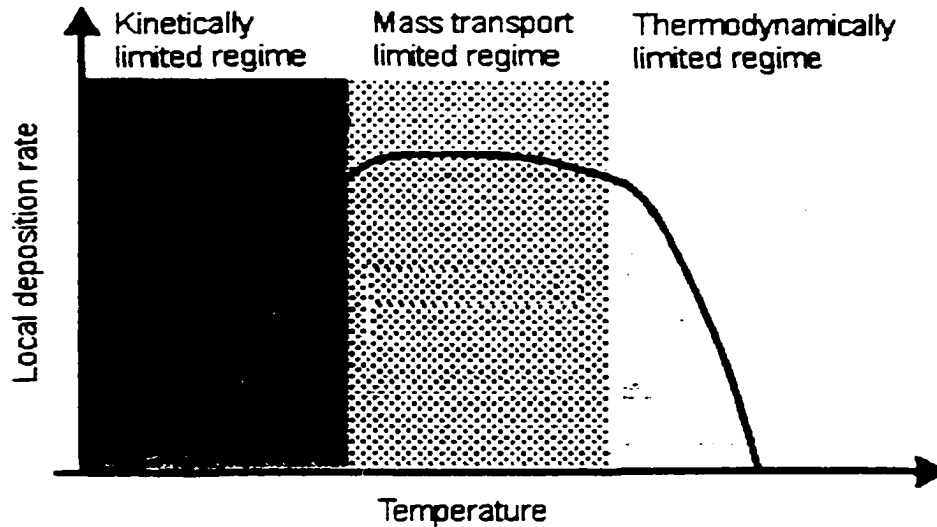


Figure 2.4 Rate-limited regimes.

2.2.1 Kinetically-Limited Regime

Usually a process is kinetically limited at low temperatures and high pressures. The reaction rate rises exponentially with increasing temperature. According to the Arrhenius relation given below, K_o is a concentration dependent rate constant, P is pressure, and E_a and R are the activation energy and the universal gas constant. Thus, at a fixed pressure, the local growth rate, R_n , is prescribed only by the surface temperature, T , and activation energy, E_a .

$$R_n = K_o(P)e^{-E_a/(RT)} \quad \text{Eqn. (2-1)}$$

2.2.2 Transport-Limited Regime

With increasing temperature, the process passes into the mass transport limited or diffusion limited regime. The surface reactions proceed rapidly, and the ability of the precursor to arrive at the surface of the reaction zone is slower than the chemical reactions. In this transport-limited regime, only large pressure and flow rate changes can affect the deposition rate in a substantial manner. The rate depends on the precursor concentration, n , which is given by diffusion equation:

$$D\nabla^2 n - \frac{\partial n}{\partial t} = 0 \quad \text{Eqn. (2-2)}$$

The solution to this partial differential equation depends on the geometry of the deposit, and diffusivity, D , of the precursor gas.

2.2.3 Thermodynamically-Limited Regime

At high deposition temperatures and low flow rates of the reaction gas mixture, the CVD reaction may rarely be limited by thermodynamics. This means that all chemicals that have entered the reactor reacts directly to form the deposit. If the flow is doubled, the deposition rate will double. The deposition yield, or the fraction of the gas phase that will react, is determined by thermodynamics.

A process can be thermodynamically limited for several reasons. Often it is caused by an increase in the apparent activation energy due to greater desorption of the precursor with temperature, i.e. the precursor desorbs before it can react. In this case the reaction rate can be described by the Langmuir-Hinshelwood equation.

$$R_n = (K_o P^2 e^{-\Delta E_a / (RT)}) / (K_{des} e^{-\Delta H_{des} / (RT)} + p)^2 \quad \text{Eqn. (2-3)}$$

Here, K_{des} and ΔH_{des} are the rate constant and enthalpies of the desorption, respectively, and P is pressure. Note that when the temperature is large (and the pressure low), the equation simplifies to an expression with the form of an Arrhenius relation with an apparent activation energy ($\Delta E_a - \Delta H_{des}$):

$$R_n = ((K_o / K_{des}) P^2 e^{-(\Delta E_a - \Delta H_{des}) / (RT)}) \quad \text{Eqn. (2-4)}$$

In addition to the constraints stated above, other constraints might also affect a pyrolytic process, such as the adsorption rate of the precursor, the desorption rate of the reaction by-products, and the nucleation rate of adsorbed species. Since these constraints follow the Arrhenius equation, they are usually included in the terminology “kinetics control of the CVD process”. For example, when adsorption limited kinetics occurs, the deposition rate is determined solely by the probability that the precursor will adsorb onto the surface. There are two types of adsorption which occur at gas-substrate surface: chemisorption and physisorption. Chemisorbed species form covalent bonds with the substrate while physisorbed species form much weaker van der Waals bonds.

2.3 LCVD Process Parameters

LCVD deposition rates are a function of many variables, such as laser power, laser diameter, laser scan rate, vapor pressure of precursors, local temperature, and thermal conductivity of the substrate. The work done by Maxwell *et al.*^[1] outlines the key parameters which determine the outcome of the LCVD process and which parameters must be controlled. Table 2.1 gives a detailed classification of various LCVD process parameters.

Table 2.1 Classification of process parameters in LCVD.

HEAT TRANSFER		
<p><u>Beam Conditions</u></p> <ul style="list-style-type: none"> • Spot geometry • Laser power • Laser intensity profile • Wavelength • Scan rate 	<p><u>Surface Properties</u></p> <ul style="list-style-type: none"> • Optical absorption, reflectivity, emissivity; refraction index • Material thermal conductivities • Surface geometry and roughness 	<p><u>Fluid Conditions</u></p> <ul style="list-style-type: none"> • Nusselt number • Reynold number • Grashoff number • Prantl number • Thermal conductivity
MASS TRANSPORT		
<p><u>Diffusion Limited</u></p> <ul style="list-style-type: none"> • Gas diffusivities • Concentrations • Size of reaction zone • Gas temperature 	<p><u>Convection Limited</u></p> <ul style="list-style-type: none"> • Sherwood number • Schmidt number • Reynolds number • Concentrations 	<p><u>Surface Limited</u></p> <ul style="list-style-type: none"> • Adsorption • Nucleation
CHEMISTRY		
<p><u>Thermodynamics</u></p> <ul style="list-style-type: none"> • Activation energy, E_a • Rate constant, K_o. 		

In the following these parameters will be described on how they may affect the LCVD process.

Laser power profile: The intensity distribution of a laser beam can vary spatially and temporally. These spatial and temporal variations in laser power determine the total amount of energy supplied for the LCVD process. For a Gaussian beam, the laser power varies radially; for a top hat beam, the power remains unchanged along the radius of the laser beam.

Laser beam diameter: The laser beam diameter is usually defined as twice the radius of the beam where the power has dropped to $1/e^2$ of the power at the beam center. The beam diameter affects the laser intensity, or laser power density, which determines the heat flux to the substrate or reactants.

Laser wavelength: The absorption of laser light on the substrate surface and/or the gas phase is to a large extent dependent on the wavelength. This means that the choice of wavelength will determine whether the process will be thermal or photolytic. The laser wavelength also affects the reflectivity on the substrate surface and, hence, the fraction of the input laser energy utilized in the LCVD process, which in turn defines the laser-induced temperature.

Scan rate: This parameter affects the laser-substrate interaction time and the size (thickness and width) and the shape of the deposited film. If the beam does not move with respect to substrate, the film is expected to deposit in the form of a dot and eventually as a rod (circular spot). On the other hand, if the beam moves relative to the substrate, the film will be deposited in the form of a line. The width of the line is affected

by the relative speed of the beam, the substrate, the laser power density, and the focused spot diameter.

Partial pressure of precursor gas or reactant concentration: The concentrations of the reactants usually influence the chemical reaction rate, which, in turn, affects the film deposition rate. As the concentration increases, the collisions between the molecules will increase, and more molecules will reach the activated state to eventually undergo chemical reaction. However, at high partial pressure, the completing adsorption with other necessary atoms/molecules may lower the reaction rate.

Physicochemical properties of the reactants: These properties affect the laser induced heating of the reactants and determine whether the LCVD process will involve photolytic or thermal reactions for a given laser wavelength.

Thermophysical properties of the substrate: These properties control the flow of laser energy in the substrate and the temperature and size of the localized hot spot on the substrate surface. It should be noted that the dimensions of the deposited film depend on the temperature and size of the hot spot in thermal LCVD.

For 3D-LCVD, Bauerle *et al.* devised a one-dimensional model that discussed the influence of different parameters on the fiber radius and laser induced temperature. The parameters investigated included laser power, spot size, activation energy of the deposition reaction, diffusion limitations in the gas phase, and temperature dependencies of the heat conductivities of deposit and the gas. Two simplified expressions for temperature and radius of the rod were arrived at:

$$T_c^2 = \frac{2APT_a}{\pi^2 \chi K_d \omega_0} \quad \text{Eqn. (2-5)}$$

$$R_s^2 = \frac{\chi AP \omega_0}{2\eta K_g T_a} \quad \text{Eqn. (2-6)}$$

T_c is the temperature at the tip, R_s is the steady state radius, P is the laser power, T_a is activation temperature, K_d and K_g are the thermal conductivity of the deposit and gas, respectively. A is the absorptivity, η is a dimensionless constant, χ is a constant defined as (R_s/ω_0) , and ω_0 is the laser spot waist radius. The calculation for laser spot waist radius can be done by either one of the following equations.

$$\omega_0 = \frac{\lambda}{\pi\phi} \quad \text{or} \quad \omega_0 = \frac{2\lambda}{\pi F} \quad \text{Eqn. (2-7)}$$

In this equation, λ is the laser wavelength, ϕ is the convergence angle of the focused beam, and F is the F-number of objective lens, which is defined as the ratio of the focal length of the lens to the diameter of the beam on the lens.

With the help of these equations, the effect of various parameters on the steady state radius of the rod and the temperature at the tip of the rod can be studied. As can be seen, an increase in laser power leads to an increase in both the tip temperature and the fiber radius, while the temperature increase is slower than that of the radius. Also, with increasing laser spot size, the tip temperature is decreased; however, the fiber radius is

increased. In other words, the reaction rate is inversely proportional to the laser spot radius.

Apparent activation energy, also known as an energy barrier that separates the energy levels of the reactants and products, plays an important role in Eqn. (2-5) and Eqn. (2-6). With increasing activation energy, the effective growth region becomes shorter, and therefore, the fiber radius decreases due to the shorter residence time above threshold. Once a deposit is formed, the temperature depends on the thermal conductivity of the deposit and the substrate and their optical properties. For example, the tip temperature may increase with decreasing thermal conductivity of the deposit due to diminished heat flux along the length of the fiber.

CHAPTER 3

LITERATURE REVIEW

The area of laser assisted chemical vapor deposition has recently been reviewed in detail by Baurele.^[12] His review, with more than 800 pages, covers the research completely until 1999. Since this state-of-the-art review is available, this chapter will be devoted to papers related to the work in this dissertation only. Some recent papers published during 2000 will also be included.

Laser Assisted Chemical Vapor Deposition (LCVD) will in this review be divided into two different categories: two-dimensional LCVD (or laser processing on a surface) and three-dimensional LCVD. 2D-LCVD has been primarily used in the direct writing of custom interconnects for integrated circuits (IC), high-level packaging, thin films, and mask repair. An example of direct writing by 2D-LCVD is illustrated in Figure 3.1. 3D-LCVD has mostly been used for prototyping microstructures. A sketch of this technique and how materials can be grown out from a substrate surface is illustrated in Figure 3.2, which shows LCVD of fibers.

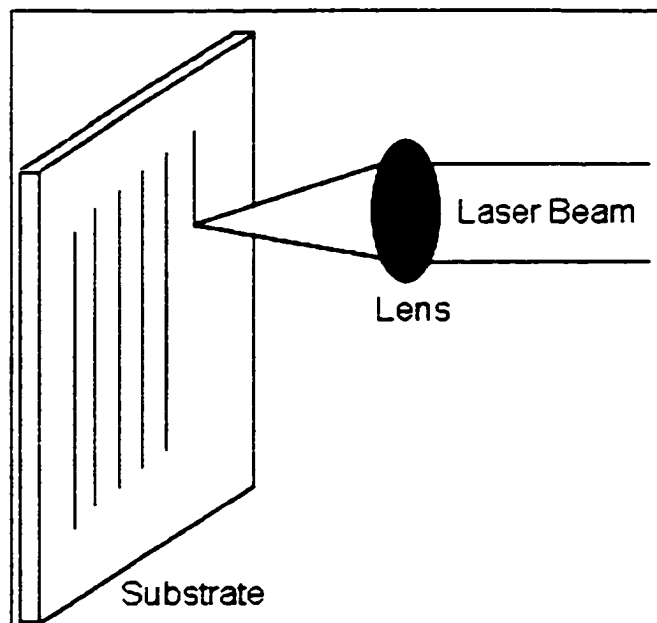


Figure 3.1 Direct writing using 2D-LCVD.

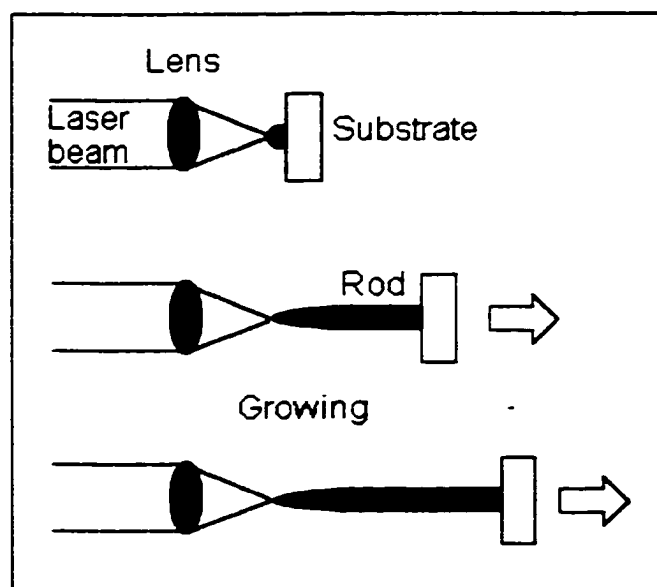


Figure 3.2 Fiber growth using 3D-LCVD.

3.1 Two-Dimensional LCVD

Most solid elements have been deposited using the LCVD techniques. The deposited elements in this dissertation include tungsten,^{[13][14]} titanium,^[15] and the substance of hafnium carbide.^[16] The work performed in this area by researchers in the past will be discussed in the following paragraphs.

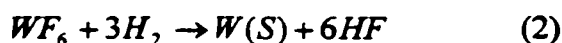
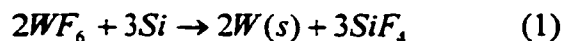
Tungsten

Tungsten is a refractory metal with a body-centered cubic structure, it has a very high melting point (3410°C), high density (19.3 g/cm³), low thermal expansion (4.45 ppm/°C), high thermal conductivity (1.73 W/cm.K at 20°C), low electrical resistivity (5.65 μΩ-cm at 20 °C), and high resistance to electromigration, all of which make it an attractive metal for surface metallization in VLSI technology. Tungsten is also a prime candidate for MEMS, see next chapter.

There are two primary precursors that have been used for the LCVD of tungsten. These are W(CO)₆, and WF₆. They have been used to deposit tungsten for packaging interconnects, for X-ray mask repair,^[17] and for gate interconnects^[14] for IC.

Tungsten hexafluoride (WF₆) is a toxic gas. When properly mixed with H₂, it is one of the fastest pyrolytic precursors known. WF₆ can be used for heterogeneous LCVD as well as for homogeneous LCVD. When silicon is used as a substrate, it reacts with WF₆ according to reaction (1) below. This reaction means that the substrate takes part in the reaction and is to some extent consumed. This reaction is self-terminating when an intact layer of tungsten is formed on silicon. In order to continue deposition of W, hydrogen or silane has to be supplied to reduce WF₆ to W according to reaction

(2).^{[10][18][19]} Alternatively, WF_6 can be hydrogen-reduced on an inert surface, such as SiO_2 according to reaction (2).



Generally speaking, there is an optimal growth rate as a function of H_2 and WF_6 molar ratio.

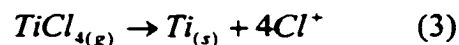
Another less used tungsten precursor is tungsten hexacarbonyl, $W(CO)_6$.^[17] This more toxic precursor requires no reducing agent and is a crystalline powder at room temperature with a melting point of 169 °C. Because the partial pressure of this precursor is lower than that of WF_6 , the maximum deposition rate is lower.^[20] The low threshold decomposition temperature of this compound, about 170°C, is its main advantage.^[21]

Recently, tungsten hexachloride, WCl_6 , was also reported to be used as a precursor for tungsten deposition.^[22] Although this precursor shows great potential having a low activation energy and reported axial growth rates of up to 3 $\mu\text{m}/\text{sec}$, the threshold temperature for deposition is relatively high at about 1500 K.^[22] Another difficulty with this precursor is that it has a very low vapor pressure at room temperature, being a solid, with melting points and boiling points of 275 °C and 346 °C, respectively.

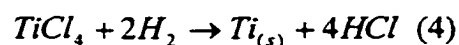
Titanium

Titanium is a high strength metal with low density (4.54 g/cm³) and excellent corrosion resistance. It has a hexagonal structure (alpha), which changes to a cubic structure (beta) at 880 °C. It has a relatively high melting point of 1660 °C. The thermal expansion coefficient is 8.5 ppm/°C at 25°C, a thermal conductivity of 0.21 W/cm.°C at 25 °C, and an electrical resistivity of 42 μΩ-cm at 20 °C.

Usually, titanium deposition is accomplished through a mixture of titanium tetrachloride, TiCl₄, and H₂.^[23] TiCl₄ is a liquid at room temperature with a high vapor pressure of 13 mbar at 20 °C and 66 mbar at 55 °C. The compound boils at 136 °C. The overall dissociation reaction is as follows:



or



Hydrogen reduction is not thermodynamically favorable pyrolysis, reaction (3) is the only way to deposit Ti from TiCl₄. It has also been reported that Ti can be deposited by photolysis using a UV excimer laser (wavelength: 248 nm) without the presence of H₂. In both cases, photolytic deposition and pyrolytic deposition need high laser powers (temperatures). The reactions, however, is fast above the temperature threshold for deposition.

Titanium tetrabromide, TiBr₄, is another precursor, which can be used for Ti deposition.^[24] This compound has a melting point of 39 °C and boiling point of 230 °C,

respectively. Relatively low deposition rate of 55 nm/s was reported using a CO₂ laser with 1 mm spot size; however, one can expect higher growth rates by reducing the spot size.^[1]

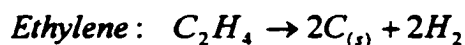
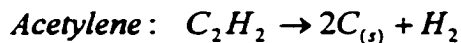
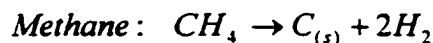
Carbon

Carbon has several allotropic forms such graphite, diamond, lonsdaleite or hexagonal diamond (a form detected in meteorites), and the recently discovered fullerenes. C₆₀ is the best known of the fullerenes. Several more or less well-defined intermediate phases between diamond and graphite also exist. They can be best characterized by the chemical bonding or the sp³/sp² carbon bond ratio. Examples of such phases are diamond like carbon and turbostratic carbon. If carbon is deposited from hydrocarbon, hydrogen often presents in the film. The hydrogen concentration, which affects the hardness of the deposit, decreases with increasing deposition temperature and is typically less than 10% for deposition temperatures higher than 1000 °C.

Carbon deposition is an important and a very active research field mainly because of the unique properties of the two polymorphs, graphite and diamond. For example, diamond may become the ultimate electronic material with its extremely high thermal conductivity, low diffusion rates, and low dielectric constant.^[25] Graphite, on the other hand, is a soft lubricating material. It has metallic conduction along the carbon layers but is an insulator perpendicular to the layers.

Precursors that have been successfully used to create carbon rods and lines include acetylene, C₂H₂, methane, CH₄, and ethylene, C₂H₄. The reaction mechanisms for

carbon deposition from these precursors are described according to the following reactions:



Several authors reported very rapid scan and deposition rates for graphite deposition. Zong^[10] reported that very large volumetric growth rates ($1.74 \times 10^5 \mu\text{m}^3/\text{s}$) could be obtained in laser assisted pyrolysis of acetylene. The substrate used in this case was SiC. Westberg *et al.*^[26] studied the relative growth of graphite from both methane and ethylene. She reported that the threshold laser induced temperature for pyrolytic deposition of carbon lines from CH_4 was 3500 K, near the sublimation temperature of graphite, 3920K. For ethylene, they reported an axial growth rate of $12 \mu\text{m}/\text{s}$ at 50 mbar C_2H_4 and a power density of $1.21 \text{ mW}/\mu\text{m}^2$. The difference in growth rate between ethylene and methane was attributed to different adsorption behavior and different stability factors of the precursors. Maxwell^{[1][27]} *et al.* also used ethylene to grow graphite rods with axial growth rate of approximately $4 \mu\text{m}/\text{s}$. His work will be discussed in 3D-LCVD section.

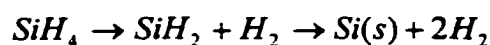
Silicon

Silicon has a density of 2.33 g/cm³, a melting point of 1410 °C, a thermal expansion of 3 ppm/°C at 25 °C, and a thermal conductivity of 1.49 W/cm.°C at 25 °C. When pure, it has an electrical resistivity of $3 \times 10^6 \mu\Omega\text{-cm}$ at 20 °C and a band gap of 1.1 eV.

Silicon is a semiconductor material, which is the basic building block of the present electronic industry. It has cubic diamond crystal structure, and its non-isotropic properties are strongly influenced by the crystal orientation. The microstructure of the deposited silicon can vary from single crystalline to amorphous depending on the deposition conditions.

Silicon is the essential structure material in both microelectronics as well as most present-day MEMS devices. This means that silicon not only possesses important electronic properties but also excellent mechanical properties especially on the microscale,^[28] including a high Q-value and a Young's modulus comparable to that of iron and steel, all of which make silicon an excellent candidate for oscillating micro-sensors and other mechanical micro-devices.

Silicon is usually laser deposited from hydrides, such as silane (SiH₄), disilane (Si₂H₆), or trisilane (Si₃H₈); sometimes, with H₂ added to the gas phase. The basic decomposition reaction of silane is as follows:



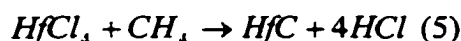
This pyrolytic reaction can be utilized by using visible lasers where no gas-phase absorption occurs. Moderate, kinetically limited, deposition rates have been observed during LCVD of silane to produce polysilicon lines.

The desire to increase Si growth rates has prompted the study of other precursors. Di-silane was found to have approximately 10 times the deposition rate of silane under otherwise identical conditions. Formation of di-silane is often the rate-limiting step in pyrolysis of silane. The most recent and promising precursor is trisilane, having approximately 60 times the deposition rate of monosilane under ideal conditions.

Hafnium Carbide

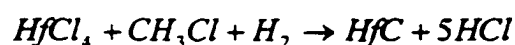
Hafnium carbide (HfC) is a refractory substance with a melting point of 3890 °C. It has a face-centered cubic (fcc) NaCl structure and a density of 12.6 g/cm³. Its composition rarely reaches the 1:1 stoichiometry because of a large inhomogeneity range, which is typical for the transition metal carbides. Because of this inhomogeneity range, HfC is normally metal rich. HfC is very hard with a Vickers hardness of 2900 kg/mm³. Its thermal conductivity is 0.08 W/cm.°C at 25 °C. Its thermal expansion is 6.6 ppm/°C at 25°C, and its electrical resistivity is low, 50 μΩ-cm at 20 °C.

The most common way to deposit HfC is to use a HfCl₄ and a hydrocarbon such as propane (C₃H₈), propene (C₃H₆), toluene (C₇H₈), or methane (CH₄) as follows.^{[29][30]}



The chloride is usually generated in situ in a generator. The reaction above has been studied over a wide range of temperatures (900-1500 °C) and pressures ranging from 10 Torr to atmospheric. Whisker formation has been observed at 1 atmosphere. and 1230 °C.^[31]

In one case, another carbon precursor, CH₃Cl, was used to deposit HfC at 1200 °C and pressure of 10-20 Torr. The overall reaction is described as the follow:



This carbon precursor has the advantage to produce a more stoichiometric HfC with a Hf/C molar ratio of close to 1.^[25]

3.2 Three-Dimensional LCVD

Nelson reported the first rod growth in literature appears in 1972 where short carbon fibers were grown from methane and acetylene. Since then, rods have been grown of aluminum, alumina, zinc, gold, nickel, tungsten, silicon, tin-oxide, and boron. In this dissertation, LCVD of carbon and tungsten rods has been studied.

Carbon

Carbon rods have been primarily grown from acetylene/hydrogen reaction gas mixture and ethylene/hydrogen mixtures. Using of methane as the carbon precursor yielded low deposition rates because of the stability of methane molecule. Bauerle *et al.*

grew rods from acetylene/H₂ and determined an activation energy of 213 KJ/mol.^[32] Later Zong^[10] grew the carbon rods, as well as rods from methane/acetylene mixtures, but found that the methane mixture yielded lower growth rates. Wallenberger^[33] reported the most impressive results produced in high pressure (above 1000 mbar of precursor) with axial growth rates up to 331 μm/sec. Wallenberger et al. found that with increasing partial pressure of CH₄ increased the deposition rate from 41 μm/sec at 3700 mbar to 331 μm/sec at 6400 mbar, while no reaction took place below 3400 mbar. This change in deposition rate using methane must be due to an increased adsorption by supersaturation in the reaction zone. The authors also experimented with ethylene at pressures of 600-3500 mbar and obtained axial growth rates of up to 125 μm/s.

More recently, Maxwell and Pegna have contributed much to the development of 3D-LCVD. In 1996 Pegna and Maxwell manufactured a sphere, an hourglass, and micron-thick needles from a variety of materials such as C, Ni, W, and Fe.^{[1][34]} Pegna *et al.* were known for their active research in growing trussed structures^[35] and micro-walled^[36] structures, shown in Figure 3.3. They also demonstrated the ability to grow rods in arbitrary directions, the ability to butt-weld independently grown rods, and the ability to build meshes continuously. Regarding the micron-walled structures they concluded that 3D-LCVD was well-suited for layered fabrication of larger volumes of micron sized structures.

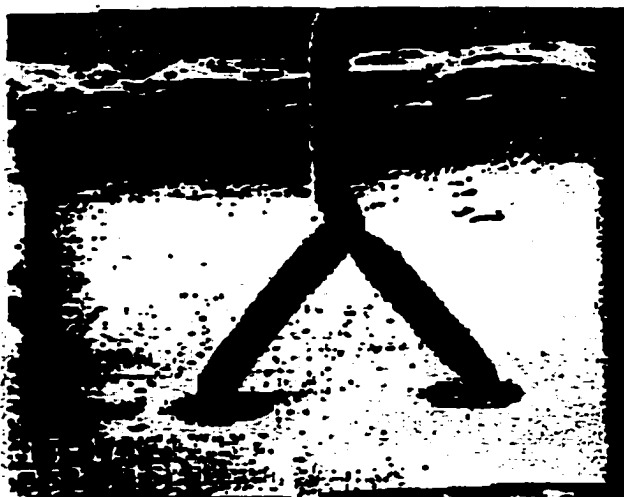


Figure 3.3 Trussed carbon structure.^[35]

Maxwell demonstrated the growth of cylindrical and tapered carbon rods on graphite substrates by varying the laser power, shown in Figure 3.4 and Figure 3.5. Recently, Maxwell *et al.*^[37] also demonstrated the growth of freestanding diamond-like carbon grown from ethylene at linear rates of up to $3.5 \mu\text{m/s}$, and helical carbon coils that are essentially highly elastic springs which can be used in low frequency response accelerometers.

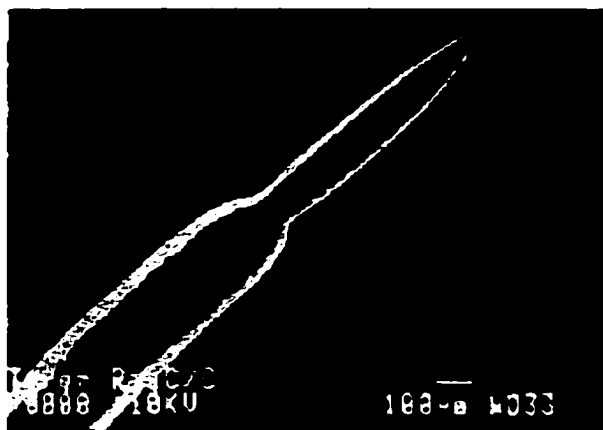


Figure 3.4 Taped carbon rods.^[37]



Figure 3.5 Diamond-like carbon microcoil^[37].

Tungsten

Allen^[38] *et al.* were the first to report the growth of tungsten rods from a mixture of WF_6 and H_2 . The partial pressures of WF_6 and H_2 were 266 mbar and 532 mbar, respectively and the rods were grown on silicon substrates. Allen *et al.* claimed that rods

40-50 μm in diameter and 50-120 μm tall could be grown at rates approaching 1000 $\mu\text{m/s}$. This very rapid axial rate has yet to be confirmed by other authors. Recently, Maxwell^[37] *et al.* reported the growth of free-standing tungsten using a wide range of laser powers. The reaction gas mixture they used was also WF_6 and H_2 , with a typical molar ratio of 1:3. They observed that at laser powers above 3.0 W, explosive, uncontrolled growth occurred. The microstructure of the deposited tungsten consisted of large grains in excess of 20 μm . At the highest laser powers, 10-12 W, multiple large crystals grew away from the substrate at oblique angles to the beam, but no rods were formed along the beam path. At laser powers below 3.0 W, fibers with single-crystalline cores and polycrystalline coatings formed, shown in Figure 3.6. Growth rate up to 160 $\mu\text{m/s}$ was obtained as a maximum.

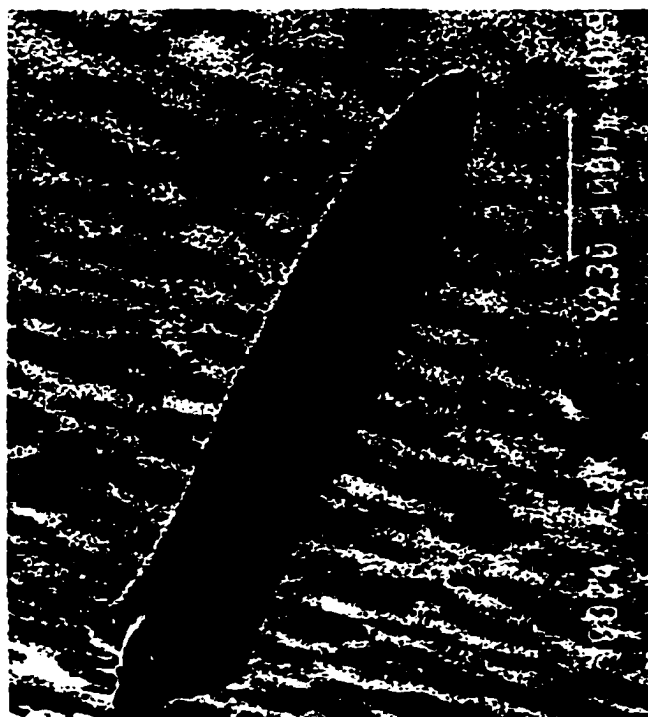


Figure 3.6 Single crystal tungsten rod.^[37]

Except for tungsten rods, Maxwell *et al.*^[37] also reported tungsten on boron microsolenoid, fabricated by laser direct writing. The tungsten lines were successfully deposited on the boron fibers, 100 μm in diameter, at a variety of scan rates and precursor partial pressures. The best results, shown in Figure 3.7, were obtained with a 1:4 mixture of WF_6 to H_2 at 100 mbar. In addition to boron-core, microsolenoids, tungsten was also deposited on 100 μm diameter Co-Fe-Si-B alloy fibers.

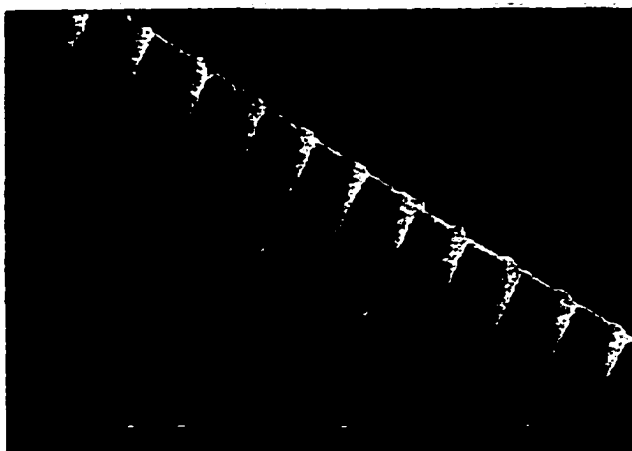


Figure 3.7 Tungsten on boron microsolenoid by laser direct-writing.^[37]

CHAPTER 4

EXPERIMENTAL SETUP AND EXPERIMENTAL PROCEDURE

In this Chapter, the LCVD system designed, assembled, and used for the experiments will be described in detail. The LCVD system is unique in its flexibility to employ a variety of precursors such as gases, liquid, or even solids. The procedure used to perform the experiments is also discussed in this chapter.

4.1 Experimental Setup

The 3D-LCVD systems consist mainly of the following subsystems: optical system, LCVD reaction chamber, vacuum system, gas-handling system, heating control system, and imaging system. The relationship among these subsystems is illustrated in Figure 4.1. A more detailed diagram of the overall system is shown in Figure 4.2. Generally speaking, the vacuum system is used to provide the necessary vacuum level for the reaction chamber during processing and it is used to evacuate by-product gases from the reaction chamber after processing. The laser provides a collimated light beam, which is focused into the reaction chamber in order to induce the chemical reaction. The gas-handling system supplies the reaction chamber with the reaction gas mixture. The heating control system is used to regulate the temperature of the reactor and the gas handling

system. This is necessary in the case some precursors otherwise would condense on the cold walls, i.e., for precursors which are liquids or solids at room temperature. The imaging system monitors the reaction process inside the reaction chamber for further data collecting and data analyzing.

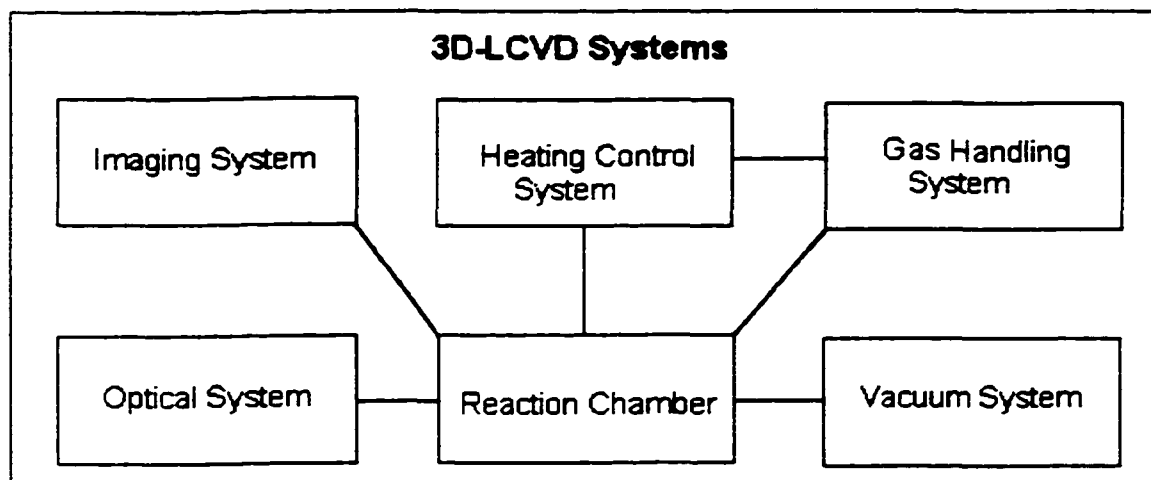


Figure 4.1 3D-LCVD subsystems.

Optical system

The optical system consists of the following components: the laser, optics, one micro-positioning stage, a thermopile detector, and a laser power meter. Throughout the experiments, a Nd:YAG laser with a maximum output power of 10 W (TEM_{00}) was employed at 1064 nm wavelength. The CW laser beam was focused by a best form laser lens with 100-mm focal length and 1 inch in diameter yielding a spot size of approximately 25 to 30 microns. The spot size can be calculated from the following equation, where in our case λ is 1064 nm and the F-number is 10. The F-number can be varied with the laser beam diameter yielding a spot with different sizes according to the needs.

$$\omega_0 = (2\lambda / \pi) \cdot F$$

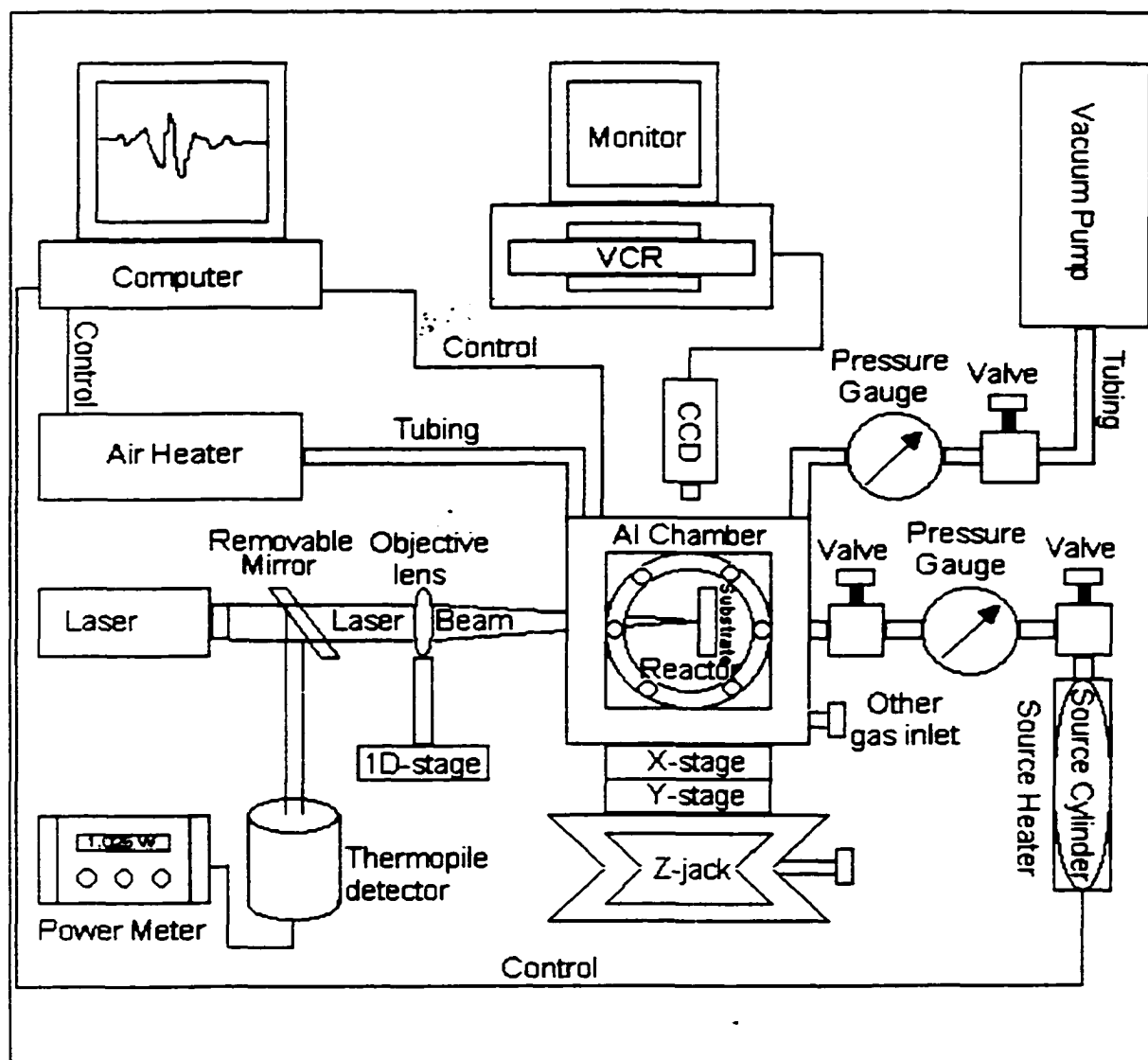


Figure 4.2 Schematic diagram of the 3D-LCVD setup.

A thermopile detector is used to collect the laser light, diverted by a removable mirror, to measure the incident laser power. The laser power is also corrected for optical losses, such as the objective lens, and several windows.

Reaction chamber

The reaction chamber consists of the reactor itself, which is enclosed in an outer aluminum chamber, which in turn is placed on a combined XY-stage, and a Z-jack stage. The reactor, shown in Figure 4.3, is essentially a spherical cube made of stainless steel that has six 1.33-inch CF ports. The inner surface of the reactor was nickel-plated to prevent corrosion from the reaction gas mixture. Two sides of the cube serve as viewports. One port was used for observation through a CCD camera equipped with a 5× objective lens. The second port served as the laser beam entrance window. The third port was dedicated for the gas delivery from the cylinder. The fourth port was connected to a vacuum pump in order to evacuate the reactor. The fifth port had a flange with a detachable substrate holder of aluminum. And the sixth port was closed with a blank flange, which could be used for future work.

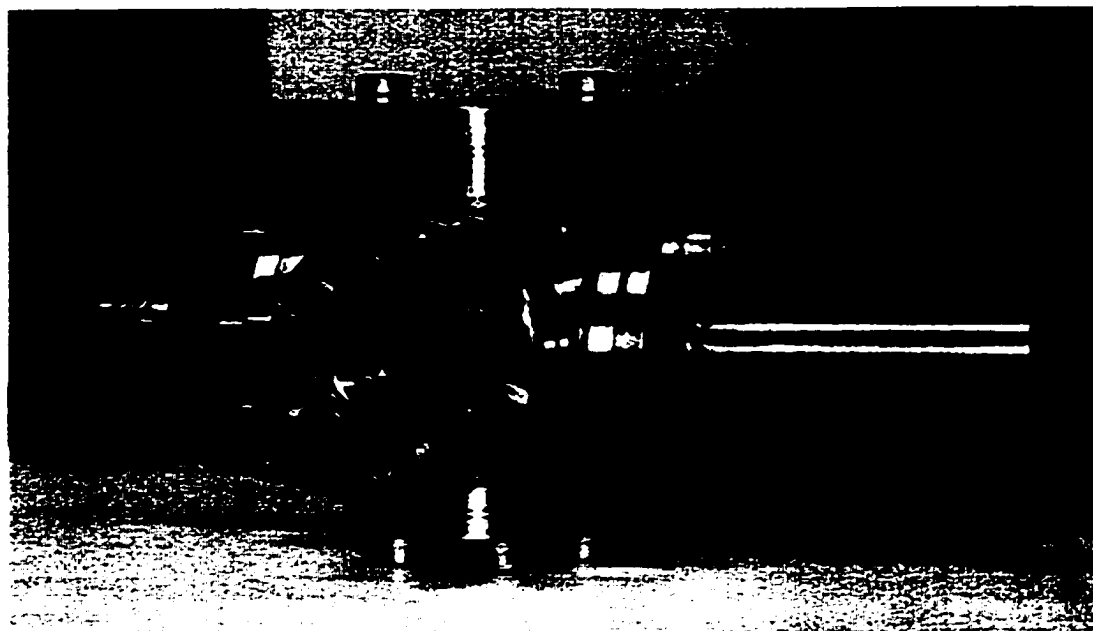


Figure 4.3 LCVD reactor.

The CF flanges are most widely used for high-vacuum and UHV applications. Flange adapters were used to connect to the gas-handling system and vacuum system through quarter-inch tubing. The view-ports, flanges, and flange adapters were mounted on the reactor using standard copper gaskets. Standard nuts and bolts secured components on the reactor. Zero-length viewports were chosen as they offer a greater distortion-free area with no interior voids that might create virtual leaks or dirt traps. The transmission characteristics are 80% minimum from 0.32 to 2.7 microns and 90% from 0.35 to 2.6 microns. The viewports used for carbon, titanium, and hafnium deposition were made from borosilicate glass and 304 stainless steel, and the viewports used for tungsten deposition are made from quartz and 304 stainless steel.

Inside the reactor, there is a substrate holder made of aluminum, custom machined in the Institute for Micromanufacturing (IfM) workshop. The shape of the substrate holder is illustrated in Figure 4.4. The substrate used for carbon deposition was a silicon wafer with a very thin coating of metal such as chromium, while the substrate used for tungsten and hafnium deposition was a tungsten wire. Tungsten was used as substrate here because of its very high melting point.

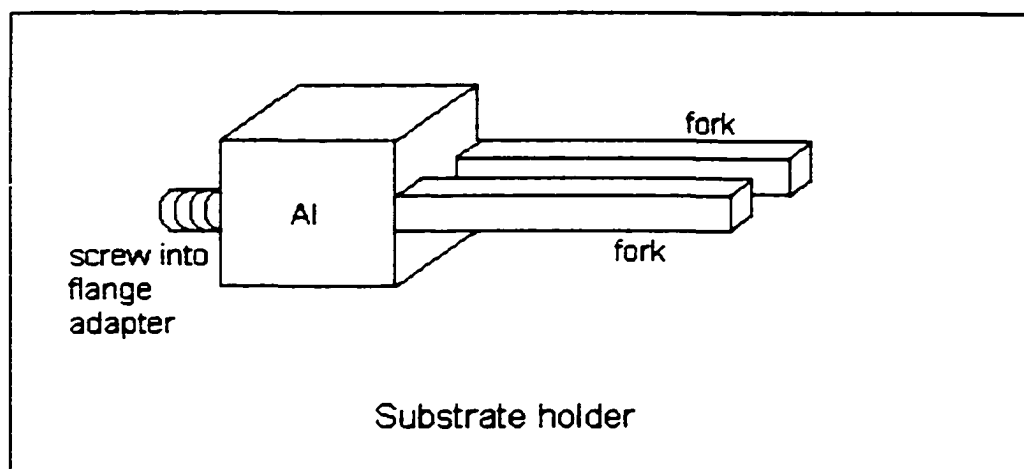


Figure 4.4 Reaction system – substrate holder.

The reactor was placed in an aluminum chamber as shown in Figure 4.5. This chamber was designed with grooves inside to let hot air flow smoothly over the reactor in order to heat it evenly. Aluminum is used in this design because of its good capacity for heat. The air inlet of the chamber is connected to the air heater, which is controlled by computer programs. A thermocouple measures the reactor temperature and feed this signal back to the computer program which adjusts the temperature at the air heater to keep the reactor at a constant temperature. This construction allows precursors having a low vapor pressure at room temperature to be heated up to temperatures above 400°C. This high temperature means that the vapor pressure for many precursors can be greatly increased.



Figure 4.5 Reaction system – aluminum chamber.

The outer aluminum chamber is then placed on an XY-stage and a Z-jack. The XY-stage here can move the substrate in a plane perpendicular to the focused laser beam. The maximum translation in the X-direction and Y-direction is 1.3 cm, which is longer than the dimension of substrate. The Z-jack, having orthogonal hinges that minimize wobble, tilting, and twisting, was meant for vertical movement and was designed to give smooth elevation up to 300 lb loads. In summary, the chamber can be easily moved in the X-Y-Z directions .

Heat-control system

The heat-control system consists of two major parts. One part is a computer with programs used to control the temperature of the air heater, the outer aluminum chamber,

and the precursor bottle. The other part is the air heater which provides a constant hot air flow throughout the aluminum chamber. The air heater has components such as a compressed air line, a flow regulator, and several heat tapes.

A precise temperature control is necessary to ensure a constant vapor pressure with time so that the partial pressure of the precursor does not change and gases do not condense in the reactor, which is especially critical on the two windows. Otherwise, condensed gases will either block the incident laser beam or blur the image captured by the CCD camera. Condensation in the reactor also means that the partial pressure of the precursor is changed. To achieve this precise temperature control, a closed-loop proportional-integral-derivative (PID) temperature control and measurement program was made using a Macintosh computer, workbench data acquisition card, and other electrical control components such as electrical relays and thermocouples. In our system, we have three separate programs to control the air heater temperature, the reactor temperature, and the precursor cylinder temperature. The PID control program is illustrated in Figure 4.6. The precursor cylinder temperature is normally set 20-30°C below the chamber temperature to prevent the above-mentioned condensation in the reactor. Also, condensation can be avoided by using a pressure gradient having a slightly higher temperature on the chamber over the precursor cylinder.

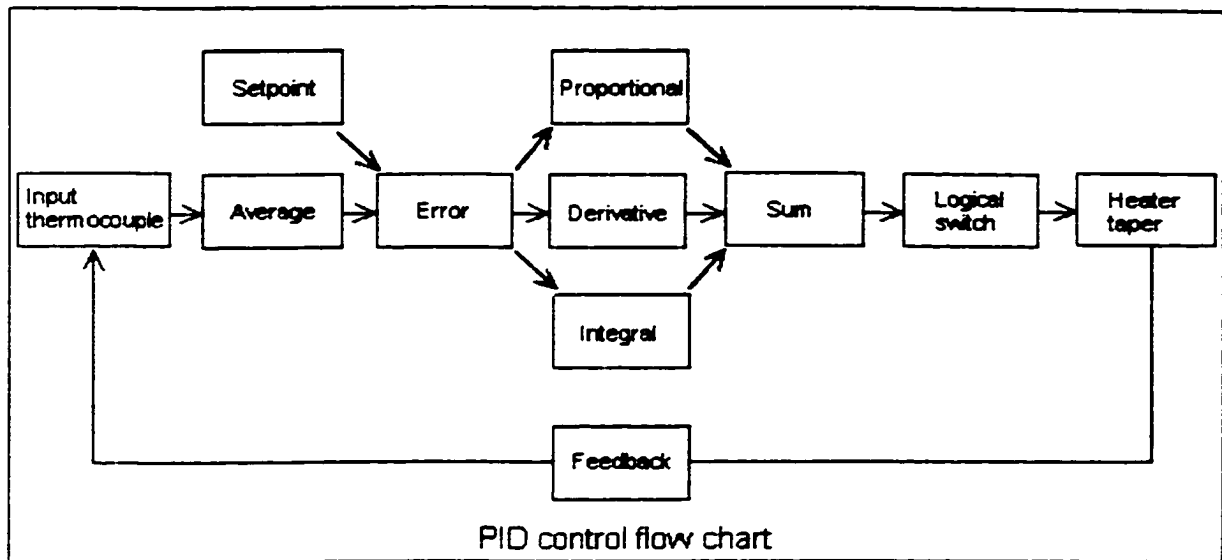


Figure 4.6 PID control flowchart.

Vacuum system

The vacuum system includes a mechanical pump, a pressure gauge, and some valves and tubing for connection. Other accessories for maintenance of the vacuum system include a helium leak detector, helium gas cylinder, and tubing. The mechanical pump is shown in Figure 4.7, and the helium leak detector is shown in Figure 4.8. The vacuum system ensures a high vacuum level in the reactor before loading precursor gases. Before any experiment, the system is leak-checked by the helium leak detector. In this system a leak rate less than 10^{-5} Torr is needed. The reasons for this are the CVD process is sensitive to impurities, and we do not want any leaks from the reactor because the precursor may be toxic or a toxic byproduct may have formed. As a preliminary test, the chamber was pumped down, sealed off, and allowed to stay for a considerable time (4 to 5 hours) without any pressure increase. Then, the equipment was leak tested both at low pressure and at pressures above atmosphere.



Figure 4.7 Vacuum system – mechanical pump.



Figure 4.8 Vacuum system – helium leak detector.

Gas-handling system

The gas-handling system provides the LCVD system with both the precursor carrying gases and other gases such as hydrogen if necessary. This system mainly has a gas cylinder, shown in Figure 4.9, a high temperature valve (can stand high temperature up to 400 °C), and connections to other gas sources.

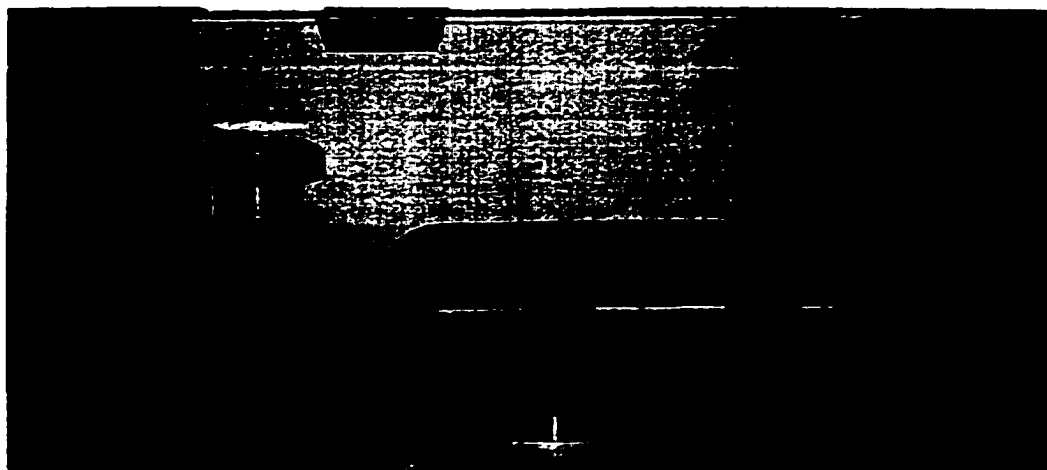


Figure 4.9 Gas-handling system – precursor cylinder.

Imaging system

The imaging system, shown in Figure 4.10, was used to in situ record and document the growth process throughout the experiment. The CCD camera with a 5 \times objective lens was connected to a video cassette recorder and a monitor. After the experiments the images recorded on the videotapes were used to determine the growth rate. Before determining the growth rate, the imaging system was calibrated against a known length standard. The monitoring equipment was also used for accurate adjustment of the laser focus.

By assembling all these subsystems, the front of the whole LCVD system is shown in Figure 4.11, except that the laser can not be seen.



Figure 4.10 Imaging system.

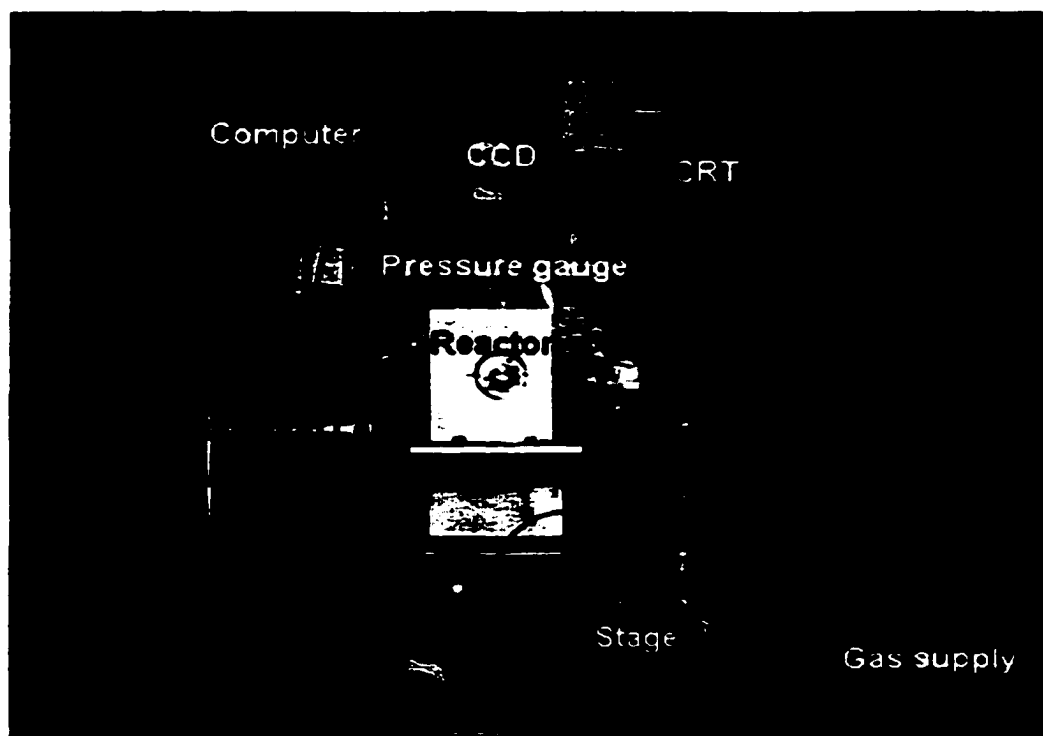


Figure 4.11 Frontview of the whole LCVD systems.

4.2 Experimental Procedure

The experimental procedure to grow rods and to discover the influence of various parameters on the growth rate basically follows the same procedure for each precursor used.

The first step is switching on the laser and locating the focus. To locate the focus, a filter is placed between the reactor's top window and the CCD camera to eliminate any stray radiation of the laser that may be reflected off the substrate. Then by adjusting the X-stage, which holds the objective lens to focus the laser beam, a characteristic glow emanated by the substrate that can be viewed on the monitor to confirm that the laser beam is focused. Finally during this step, we move the focal point about 200-250 microns in front of the substrate and turn on the laser to the power needed for deposition and the desired precursor is added. The rod starts to grow, first slightly out of focus. The growth rate is measured when a 250 μm long rod has developed which is at the focal point at the highest laser-induced temperature. By doing it in this way the non-steady state conditions prevailing during the initial stages of growth can be avoided.

All precursors (i.e. propyne, butyne, pentyne, hexyne, octyne, titanium tetraiodide, hafnium tetrachloride, except tungsten hexafluoride) were loaded into the precursor cylinder in a dry-box environment, a nitrogen-purged atmosphere. First, the dry-box was purged several times with nitrogen to drive out any oxygen or traces of residual gases therein, thereby ensuring that the loading of precursors in the source cylinder takes place in a completely inert atmosphere. All the precursors, except propyne, are either in liquid form or in solid powder form, and they are poured into the source cylinder through a funnel custom made to fit the size of the source cylinder opening.

After the cylinder was loaded, the opening of the source cylinder was closed, and the dry-box was again purged with nitrogen. This procedure ensured the elimination of any traces of the precursors that might escape into the atmosphere while removing the source cylinder from the dry-box. As for propyne and tungsten hexafluoride, they were available as gas cylinders, so they could be directly connected to the reactor.

Once the precursor had been loaded in the source cylinder and connected to the reaction chamber, it was evacuated for several seconds by quickly opening and closing the valve. This step evacuated the nitrogen inside the cylinder. Then, the cylinder, valves, and tubing were wrapped with aluminum foil and heater tapers.

The temperature of the source cylinder defines the vapor pressure of each chemical. Again, the reactor and tubing were heated to about 20-30°C higher than that of source cylinder to eliminate condensation of the precursor in the reactor during the experiments. The source cylinder is heated after that the reaction chamber has reached the preset temperature. During this entire operation, the chamber is evacuated several times to remove any residual gases. When the source cylinder reaches its preset temperature, the valve between the source cylinder and the reactor is opened permitting the gas to fill up the reactor. Once the pressure gauge reading confirms a sufficient pressure exerted by the vapor phase of the gas, the laser is switched on, and experiments are then performed. Figure 4.12 shows an example of carbon rods grown on the silicon substrate.



Figure 4.12 An example of carbon rods grown on silicon substrate.

To ensure the consistency in the experiments and to obtain reliable results from each precursor, the rods were allowed to grow through the depth of the focus. The growth rate was measured from microscopic video footage along the fiber to find the highest rate. Ten to twelve measurements were made along the steady-state growth of each rod. The time taken for this rod to transverse this distance was noted. The peak rate along these readings was then reported for each rod at corresponding laser powers and vapor pressures. The pressure was directly read from the pressure gauge connected-close to the reactor. After the rods have been grown, each rod is measured using the scanning electron microscopy (SEM) (AMRAY 1830), shown in Figure 4.13. This instrument gives an accurate value of the length and diameter of each rod.

Two types of experiments were conducted on the alkynes, namely (a) Growth rate as a function of partial pressure where all other parameters were held constant (laser

power); and (b) growth rate as a function of laser power where all other parameters were held constant (pressure). The laser powers employed were in the range of 0.4 W to 1.5 W, and the pressure range used was from 500 mbar to 3000 mbar. These values were typical for carbon growth. Different laser power and pressure conditions were used for refractory metals' deposition (W and HfC), and which will be discussed in more detail in the next chapter.



Figure 4.13 SEM – AMRAY 1830.

After a run with a particular precursor, the reactor was evacuated directly, either to the exhaust or the vacuum pump depending on the precursors used. The reaction system and the gas-providing system were cleaned from time to time to ensure good experiment results.

CHAPTER 5

RESULTS AND DISCUSSIONS

5.1 Deposition of Carbon from Alkynes

5.1.1 Growth Rate as a Function of Laser Power

In these experiments, the pressure inside the reactor was held constant at 1000 mbar, and the laser power was varied from 0.4 W to 1.5 W. The steady state axial growth rate as a function of laser power and for each precursor is presented in Figure 5.1. The growth rate was measured in microns/sec, the rod diameter in microns, and the laser power in watts.

It can be observed from Figure 5.1 that the growth rate of each alkyne passes through 2 regions: (a) from 0.4 W to about 1 W, where the growth rate increases exponentially with increasing laser power; and (b) from 1 W to 1.5 W, where the growth rate increases linearly with increasing laser power. The exponential dependence indicates a kinetically controlled region. This is typical at low laser powers i.e., temperatures, where surface chemical reactions are the rate limiting processes. The reason for this exponential increase follows the Arrhenius equation that describes the growth behavior in the kinetically limited region. This equation can be expressed as the following:

$$GR = Ae^{\frac{-E_a}{RT}} \quad (1)$$

In equation (1), GR is the growth rate, A is the pre-exponential factor, E_a is the apparent activation energy, R is the general gas constant, and T is the temperature. Since the laser power is roughly proportional to the laser-induced temperature, it follows that the growth rate is exponentially dependent on this variable.

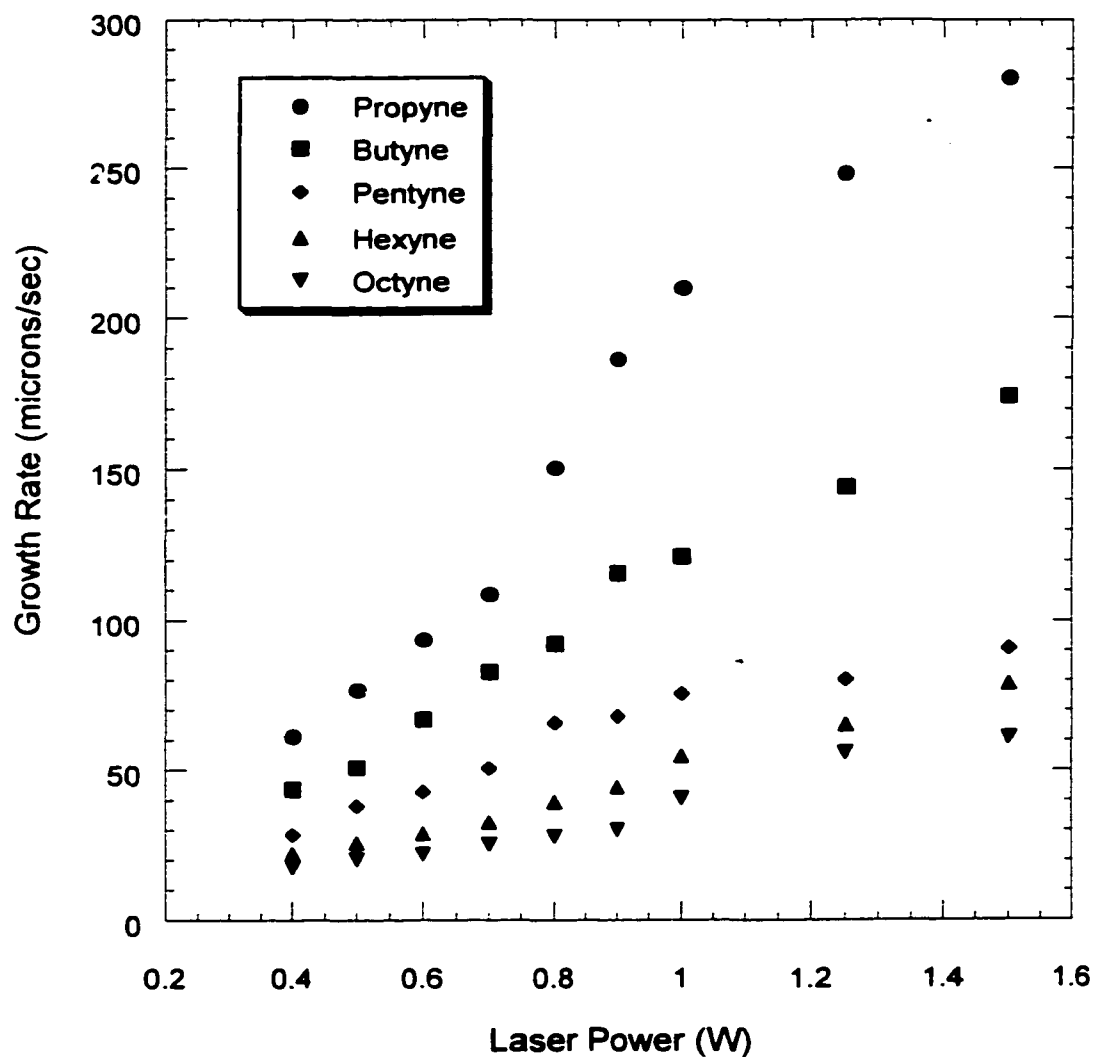


Figure 5.1 Growth rate as a function of laser power for alkynes.

Figure 5.2 shows the exponential curve fit for the growth rates of the different alkynes from 0.4 W to 1.0 W. These curves were fit to an Arrhenius-like equation:

$$GR = Ce^{BP} \quad (2)$$

Here P is the laser power.

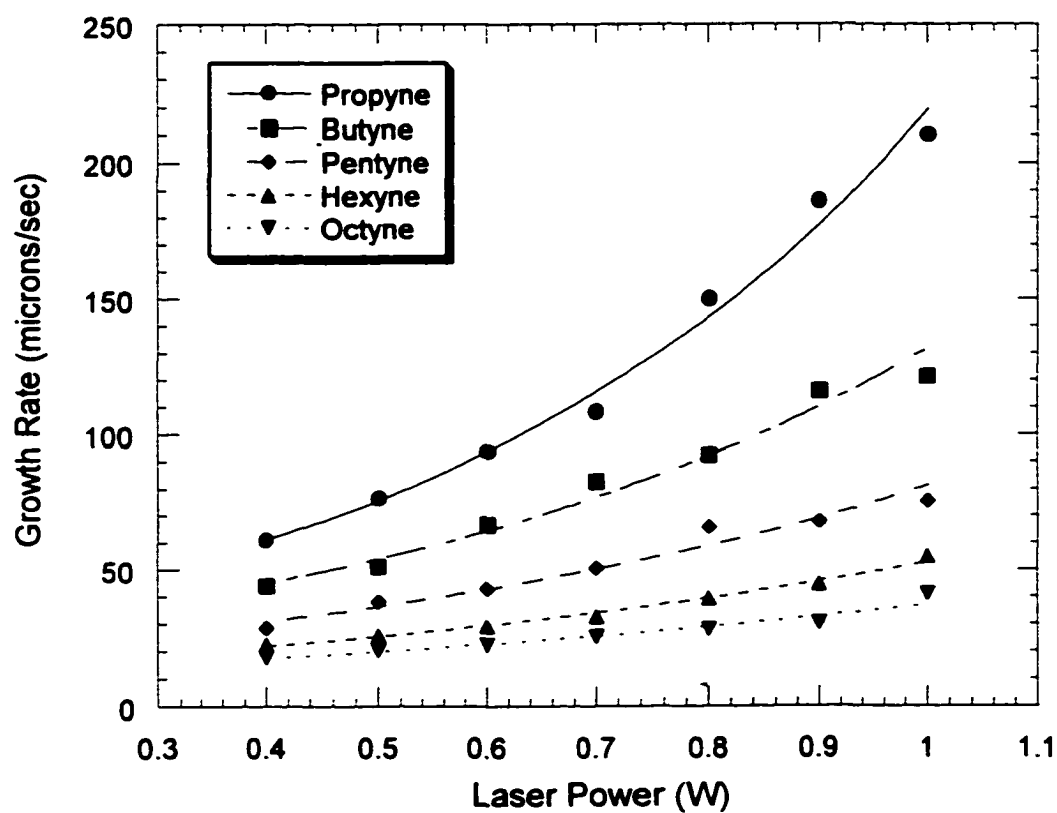


Figure 5.2 Curve-fit for exponential region – alkynes.

It can be seen from Figure 5.2 that the constant B in equation (2), which is how steep the curves increase with laser power, decreases with increasing molecular weight of

the precursor. The decreased constant B indicates that the apparent activation energy decreases with the molecular weight of the alkyne, and which is probably because the stability of the alkynes decreases with increasing molecular weight.

From the data and the fits in Figure 5.2, it was also found that the constant A decreases as a function of the molecular weight of the alkyne. This observation is valuable information since the constants C and B in equation (2) can be used to predict the behavior of the deposition process. If high deposition rates are important, both C and B should be high, which means that a small increase in laser power means a large increase in deposition rate. If, on the other hand, an easy-to-control process is wanted, B should be small. This small B corresponds to a low apparent activation energy of the process. Such processes are not so temperature sensitive, i.e. small variations in laser power will not affect the growth rate as much as that of a process having a high apparent activation energy.

The linear dependence in the region between 1 and 1.5 W in Figure 5.1 indicates a mass transport limited process. A linear curve-fit for this region is shown in Figure 5.3. The linear dependence is frequently observed in deposition processes at high temperatures (i.e. in this case when the laser power reaches 1 W), where the chemical reactions proceed rapid enough and the transport or diffusion of the reactants to the surface becomes the limiting process. Usually this dependence follows a $T^{-1.5}$ dependence, or in this case, a $P^{1-1.5}$ dependence. From Figure 5.3, we also can see that the longer the carbon chain, the smaller the growth rate increases as a function of laser power. This observation can be attributed to the lower diffusion coefficients of alkynes with higher molecular weight.

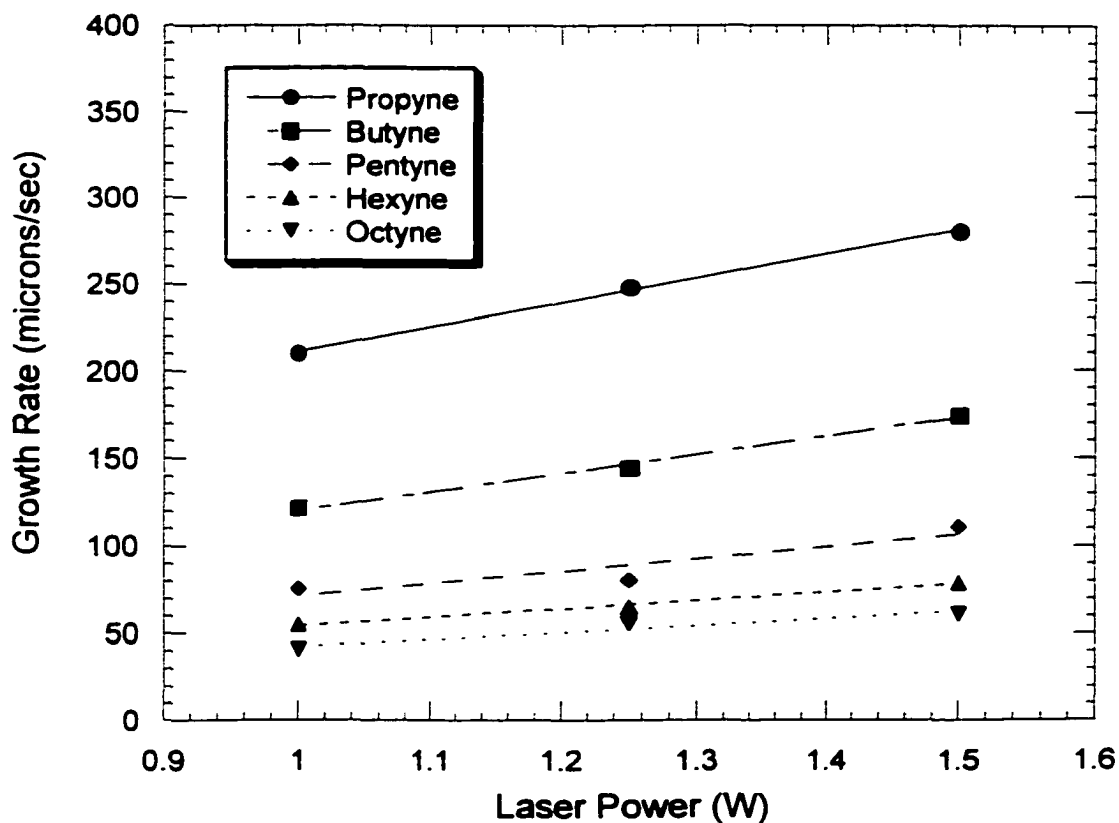


Figure 5.3 Curve-fit for linear region – alkynes.

The microstructure depends on both pressure and temperature. As we move from a lower temperature to a higher temperature, the microstructure changes from amorphous to small-grained to larger-grained (polycrystalline). Finally, at high enough temperatures, single crystal growth may be obtained. The effect of the pressure dependence is more complicated. Usually as we increase the pressure, the microstructure usually changes from a single crystalline to a polycrystalline and finally to an amorphous structure. This variation in microstructure as a function of process parameters is frequently observed in CVD and LCVD processes. An increase in laser power or laser-induced temperature means that the surface diffusion on the laser heated area increases, which in turn will

increase the size of the crystals in the growing material. An increase in deposition rate at constant temperature means that the crystallite size will decrease since the residence time of the adsorbed species on the laser heated area will be shorter, i.e., the different species on the surface will have less time to diffuse.

Some typical rods that illustrate the discussion above are shown in the following figures below.

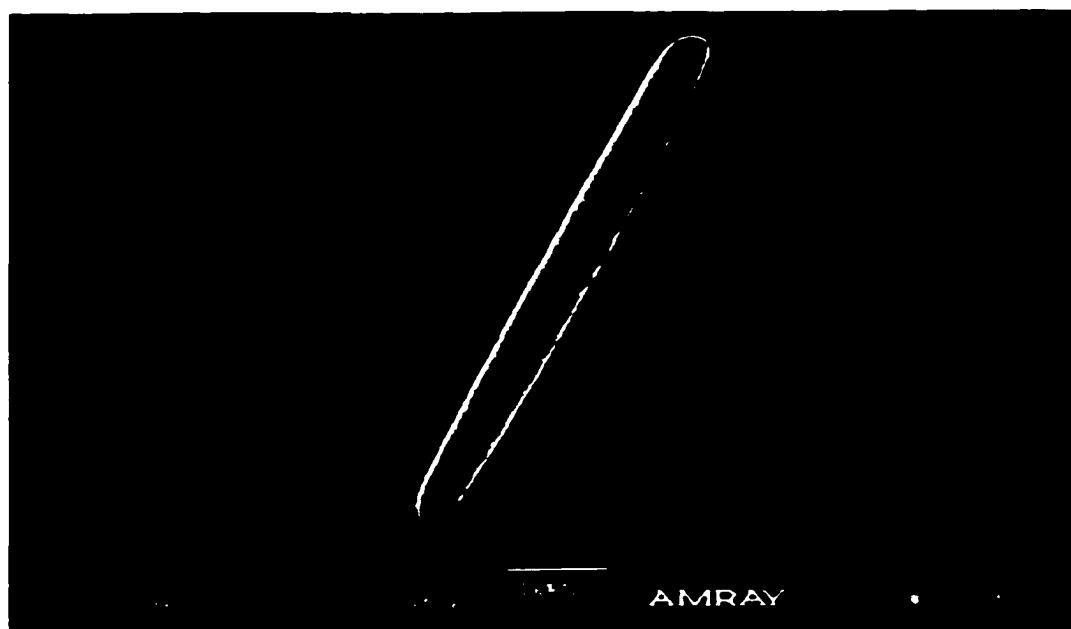


Figure 5.4 Smooth amorphous rods – low powers.

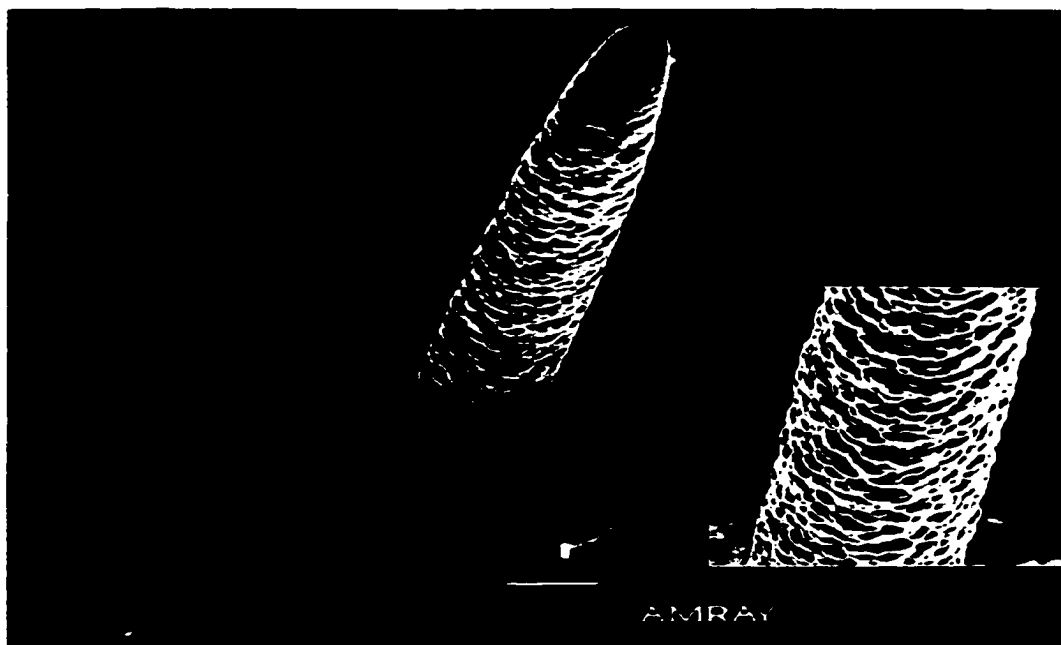


Figure 5.5 Polycrystalline (small grains) rods – middle power.

Some observations from this section are summarized as follows.

- (1) The propyne growth rate increased from 61 $\mu\text{m}/\text{sec}$ at 0.4 W to 280 $\mu\text{m}/\text{sec}$ at 1.5 W.
- (2) The butyne growth rate increased from 44 $\mu\text{m}/\text{sec}$ at 0.4 W to 174 $\mu\text{m}/\text{sec}$ at 1.5 W.
- (3) The pentyne growth rate increased from 28 $\mu\text{m}/\text{sec}$ at 0.4 W to 100 $\mu\text{m}/\text{sec}$ at 1.5 W.
- (4) The hexyne growth rate increased from 22 $\mu\text{m}/\text{sec}$ at 0.4 W to 80 $\mu\text{m}/\text{sec}$ at 1.5 W.
- (5) The octyne growth rate increased from 18 $\mu\text{m}/\text{sec}$ at 0.4 W to 61 $\mu\text{m}/\text{sec}$ at 1.5 W.

5.1.2 Growth Rate as a Function of Pressure

In these experiments, the laser power was maintained at 450 mW, and the pressure was increased from approximately 500 mbar to about 3000 mbar. The results for the alkynes are shown in Figure 5.6. It can be concluded from this Figure that the growth

rate depends in a non-linear way on the precursor pressure excluding a linear reaction order.

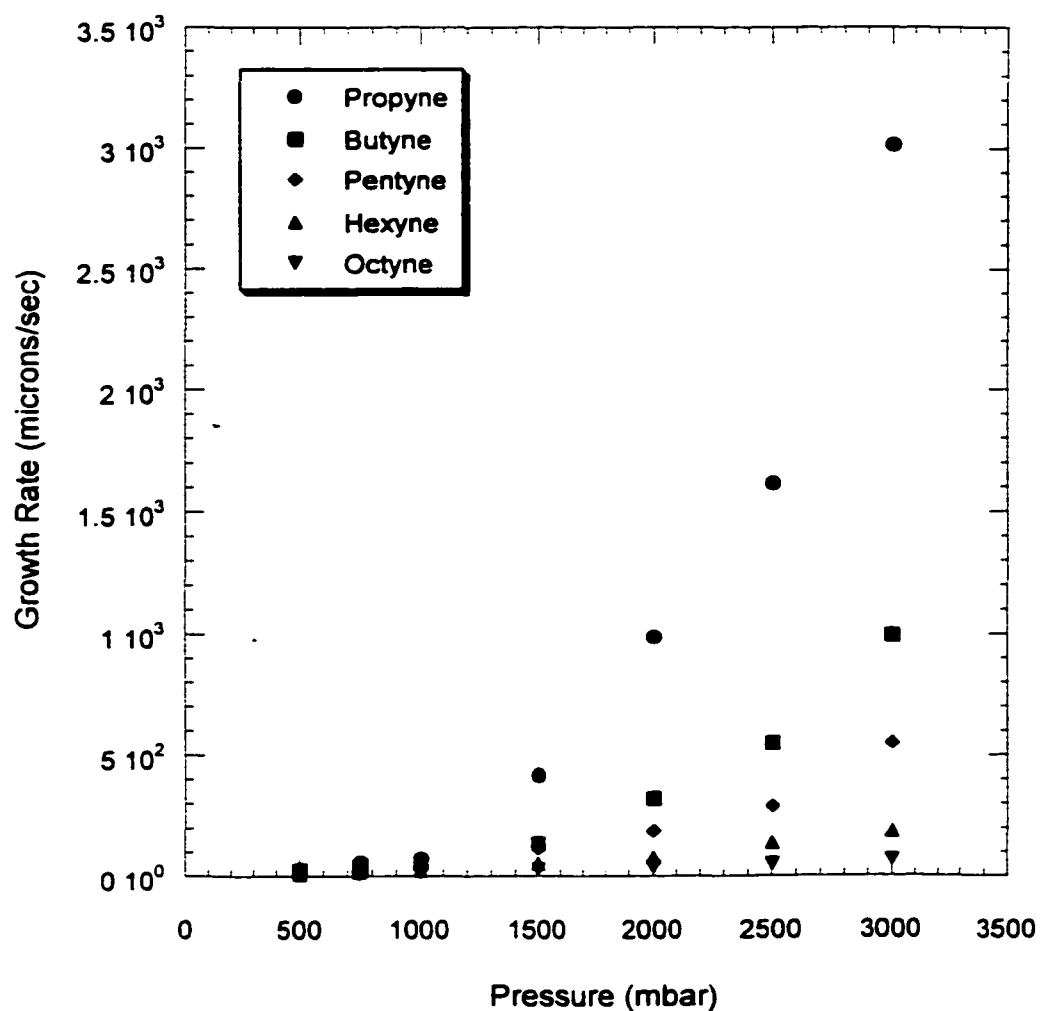


Figure 5.6 Growth rate as a function of partial pressure for alkynes-linear.

The reaction order, X , is defined by the following equation:

$$r = k \cdot P_i^X \quad (3)$$

Here, r is the deposition rate, k is a constant, and P_i is the partial pressure of the alkyne. The reaction order of a non-linear reaction can be easily derived if the data in Figure 5.6 is plotted on a log-log scale (see Figure 5.7). Then the equation (3) can be transformed to equation (4):

$$\log r = \log k + X \log P_i \quad (4)$$

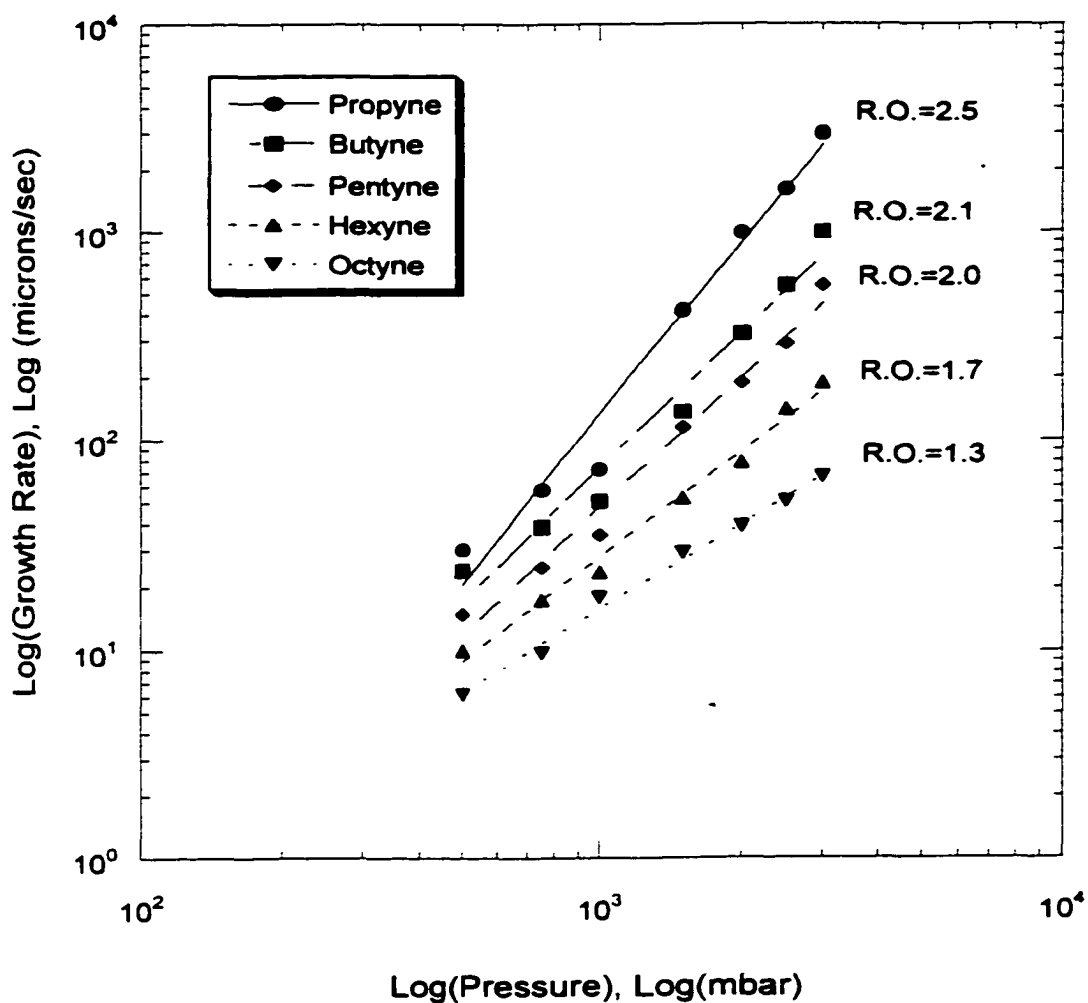
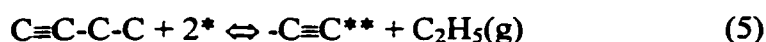


Figure 5.7 Growth rate as a function of pressure for alkynes-logarithm.

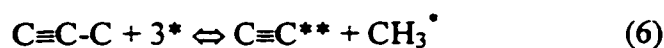
The slope of the curves in Figure 5.7 is thus the reaction order for each alkyne. As can be seen from Figure 5.7, the slope of the curves increases with decreasing molecular weight of the alkyne. In other words, the slope of propyne (2.5) is greater than the slope of butyne (2.1), which in turn is greater than the slope of pentyne (2.0), hexyne (1.7), and octyne (1.3). The reaction order for such relatively complex molecules as the alkynes is a complicated function of the deposition mechanism. If all elemental reaction steps in the deposition mechanism of a specific alkyne proceed serially, the apparent activation energy and the reaction order may reflect the rate-limiting step.

For instance the reaction order of butyne which is close to 2 could indicate the following rate limiting step (no hydrogen is included):

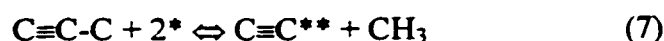


Here, * is an adsorption site on the growing carbon surface. Reaction (5) means that butyne is dissociatively adsorbed on the surface. $-\text{C}\equiv\text{C}$ stays on the surface and is incorporated in the growing carbon matrix. C_2H_5 is expelled from the butyne molecule during adsorption.

Propyne could be dissociatively adsorbed on the surface according to the following formula:



Or



In both cases, a $C\equiv C$ fragment and a methyl radical are formed. In reaction (6) the methyl radical is adsorbed on the growing surface and may react further to carbon, which is incorporated in the growing rod. According to reaction (7) the methyl radical is simultaneously desorbed during the adsorption of propyne. Both processes may compete with each other resulting in a reaction order of 2.5. As always in kinetic investigations the mechanism is guesswork. In this case several more investigations have to be made. In order to predict a mechanism, the temperature has to be controlled better. The composition, i.e., the amount of hydrogen incorporated in the carbon rods is important information, as well as the type of bonding between the carbon atoms in the rods.

Below is a summary of the growth rate obtained at minimum and maximum partial pressures, respectively. The highest deposition rate observed was more than 3.5 mm/s. The growth rate for each precursor at two different partial pressures is shown in Table 5.1.

Table 5.1 Growth rate range for each alkyne in constant pressure experiments.

Precursors of alkynes	Growth Rate ($\mu\text{m}/\text{sec}$)	
	Pressure=500 mbar	Pressure=3000 mbar
Propyne	30	3515
Butyne	24	995
Pentyne	15	548
Hexyne	10	187
Octyne	6	67

5.1.3 Rod Diameter as a Function of Laser Power

The diameters of the rods were measured and plotted as a function of laser power as shown in Figure 5.9. The partial pressure of precursor was kept constant at 1000 mbar. Two regions of growth can be identified in Figure 5.9. Near the onset, the deposition rate is strongly dependent on the physical and chemical properties of the substrate material. This onset deposition regime is a transient regime. In the stage of steady-state growth, characterized by a constant rod diameter, shown in Figure 5.8, the deposition depends on the laser power, the concentration of reactants, and on the physical properties of the deposit (reflectivity and thermal conductivity), but not on the substrate material.

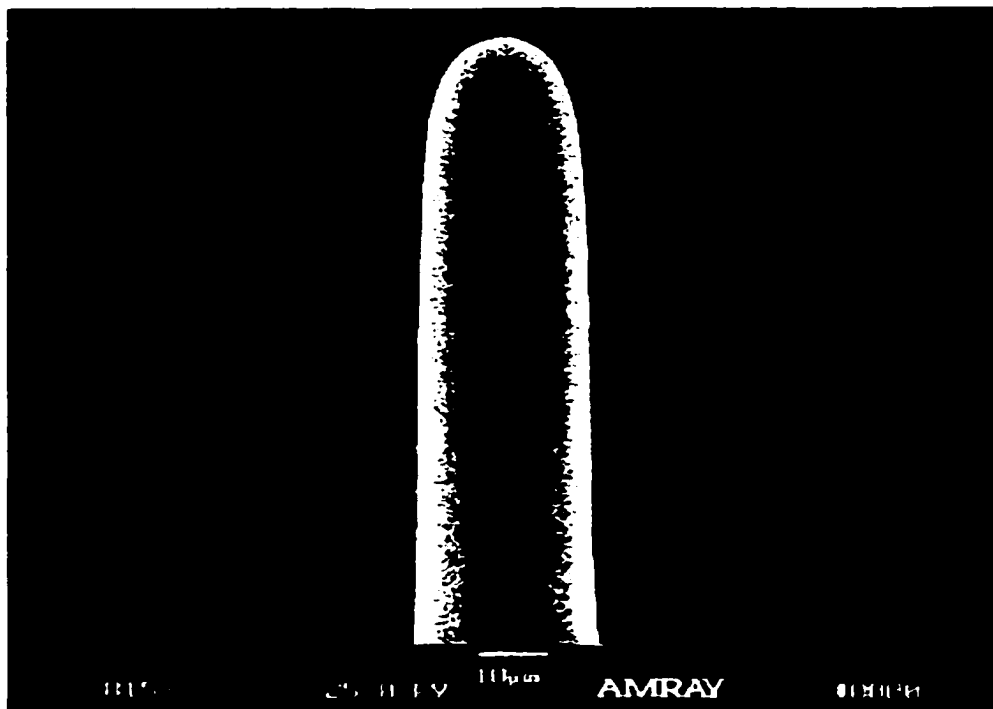


Figure 5.8 Rod of constant diameter with smooth surface.

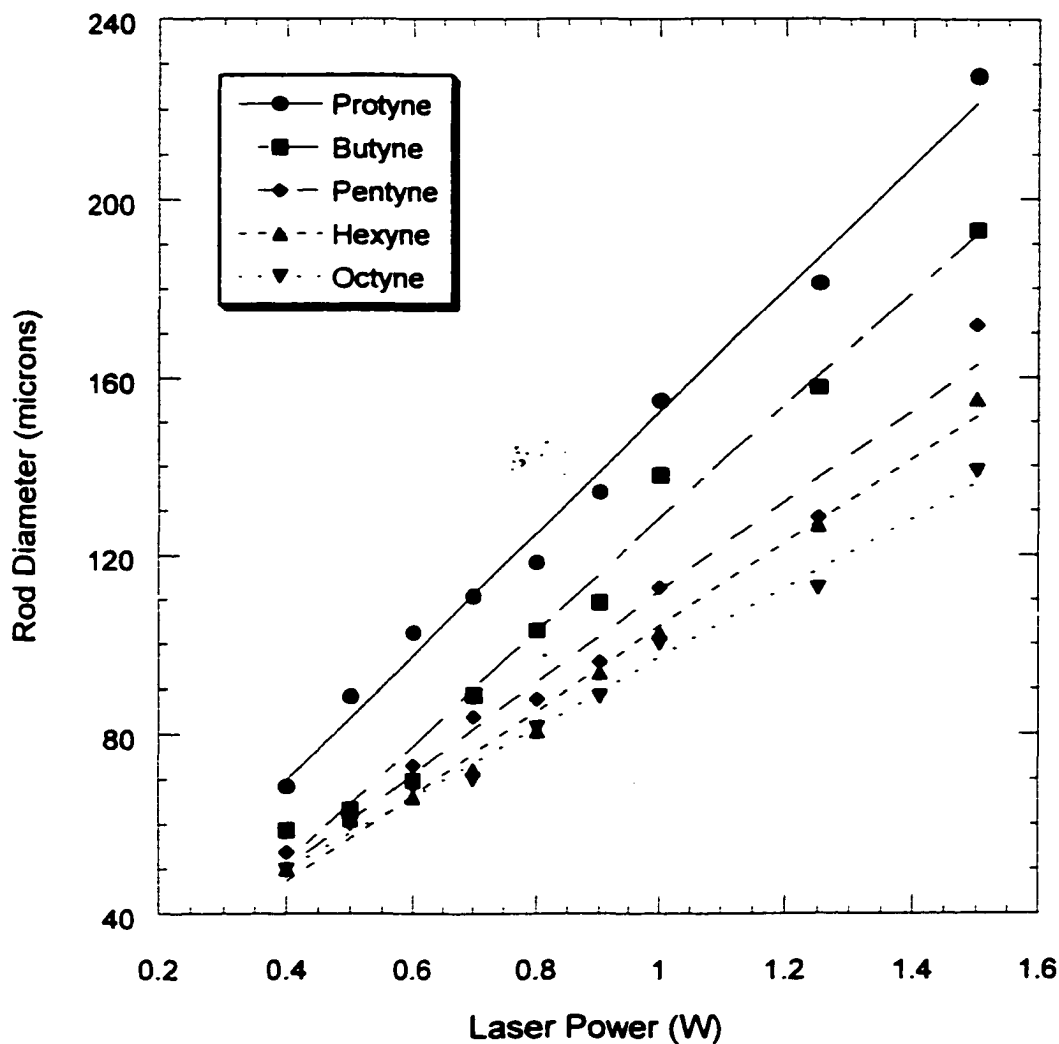


Figure 5.9 Rod diameter as a function of laser power for alkynes.

From Figure 5.9, we can see that the rod diameter increases linearly with increasing laser power for each alkyne. The slope of the curves in Figure 5.9, i.e., the rate with which the rod diameter grows, decreases with increasing molecular weight of the alkyne. The decreased slope means that the heavier the alkyne, the thinner is the rod at the same laser power. This observation is probably coupled to several factors as follows:

1. The laser induced temperature. The higher the laser power, the higher the laser induced temperature. The laser induced temperature distribution widens with increased temperature, illustrated in Figure 5.10. The widened temperature distribution will in turn lead to a thicker rod and explains the general trend with increasing rod diameters as a function of increasing laser power.
2. The axial growth rate of the rod. The higher the axial growth rate, the thicker the rod. Propyne has the highest axial growth rate, which is higher than all other alkynes at the same laser power and partial pressure. The higher axial growth rate of propyne explains why the slope of propyne is higher than that of butyne. All the slopes in Figure 5.9 can be explained in a similar way.
3. The activation energy affects the size or the shape of laser grown objects. The higher the activation energy, the thinner the rods tend to be. This phenomenon is also illustrated in Figure 5.11. Since propyne has the highest activation energy, it would be expected to form the thinnest rods of all the alkynes. But it is not the case we observed, probably because the difference in activation energies between alkynes is small.

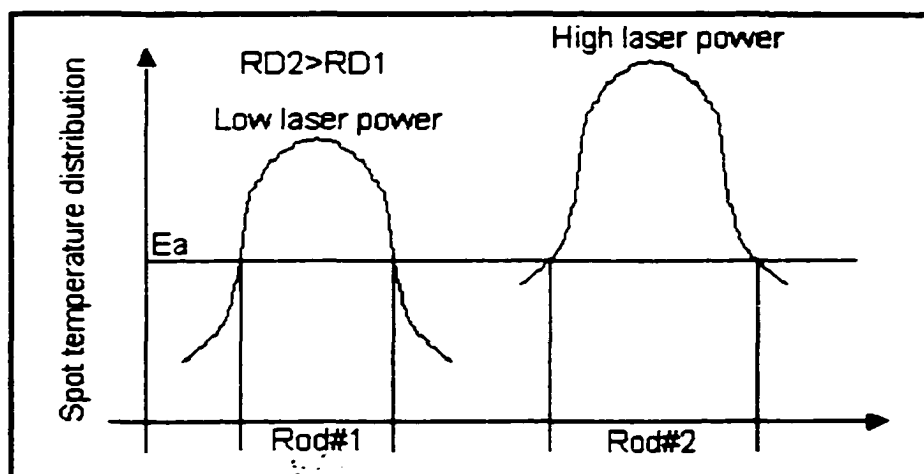


Figure 5.10 Relationship between temperature distribution and rod diameter.

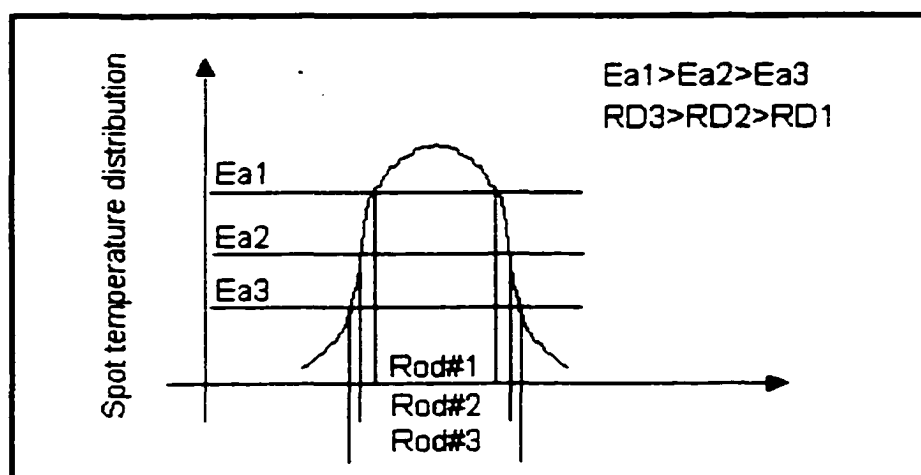


Figure 5.11 Relationship between activation energy and rod diameter.

5.1.4 Rod Diameter as a Function of Pressure

A constant laser power of 0.45 W was used throughout the experiments while the partial pressure of the alkyne precursors was varied from 500 mbar to 3000 mbar.

The complicated relationship between rod diameters and precursor partial pressures are shown in Figure 5.12. One general trend is that the rod diameter first

increases when increasing partial pressure from 500 mbar to 1000 mbar. Increasing the partial pressure further means a drastic decrease in rod diameter for propyne, butene and pentene. For propyne the diameter decreases from about 100 μm at 1000 mbar to less than 40 μm at 3000 mbar. For hexyne and octyne, the rod diameters are roughly constant with increasing partial pressure. One explanation for the decrease in rod diameter with increasing partial pressure would be because of the cooling effect of the pressure increase. On the other hand, this cooling effect would also present in the axial growth rate curves in Figure 5.6. Since this cooling effect is not the case from our observation, a more complicated mechanism is probably responsible for the trends in Figure 5.12. A further investigation, including density measurements of the rod to rule out density variations, is needed. Table 5.2 summarizes the results in Figure 5.12.

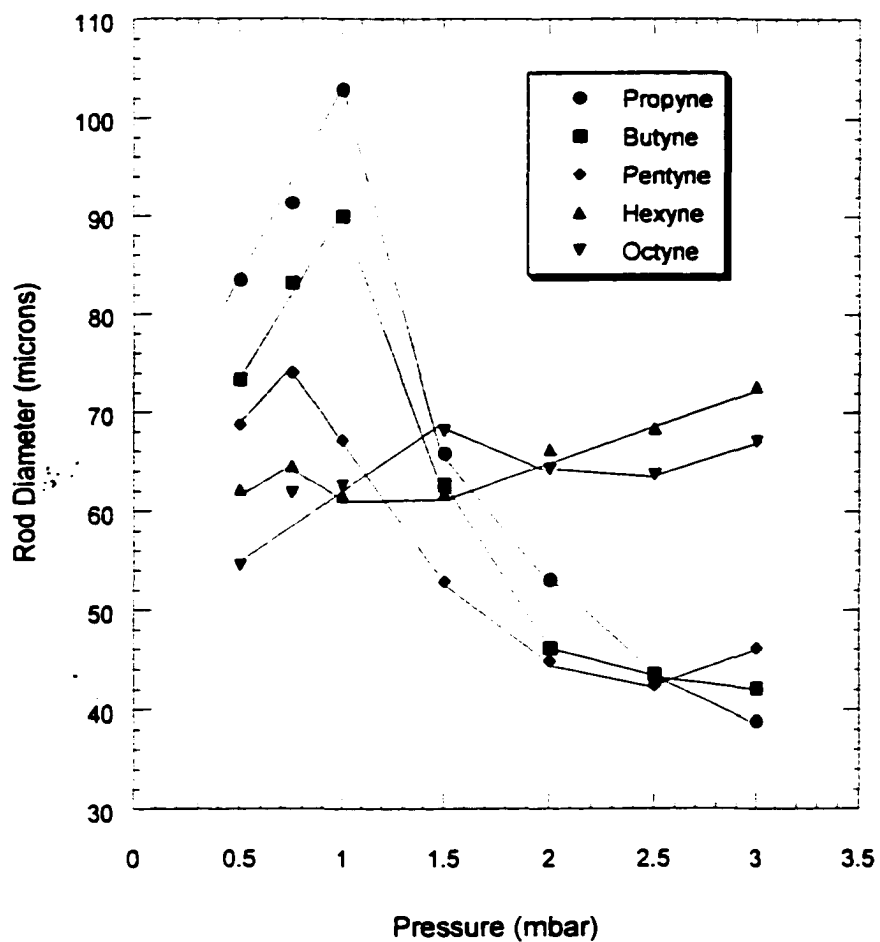


Figure 5.12 Rod diameter as a function of partial pressure for alkynes.

Table 5.2 Rod diameter range for constant laser power experiments.

Precursors of alkynes	Rod Diameters (μm)	
	Minimal	Maximum
Propyne	38	103
Butyne	43	90
Pentyne	42	74
Hexyne	61	72
Octyne	54	68

In order to gain more information about the pressure dependence, the volumetric growth rate as a function of precursor partial pressure was plotted both linearly and logarithmically in Figure 5.13 and Figure 5.14, respectively. From Figure 5.13, it can be seen that the volumetric growth rate of each precursor is non-linearly dependent on the partial pressure. From Figure 5.14, two linear regions can be distinguished irrespective of which precursors. The first region is at pressures below 1000 mbar having a slope of 2.1, and the other region is at pressures above 1000 mbar having a slope of 1.2. The strong increase in volumetric growth rate with increasing partial pressure until 1000 mbar can be explained by the fact that both the linear growth rate and the thickness of the rods increase in this pressure region. At higher partial pressures the linear growth rate increases, but the rod diameter decreases with increasing partial pressure of the alkynes. These explanations can account for the smaller slope at the pressure region of above 1000 mbar.

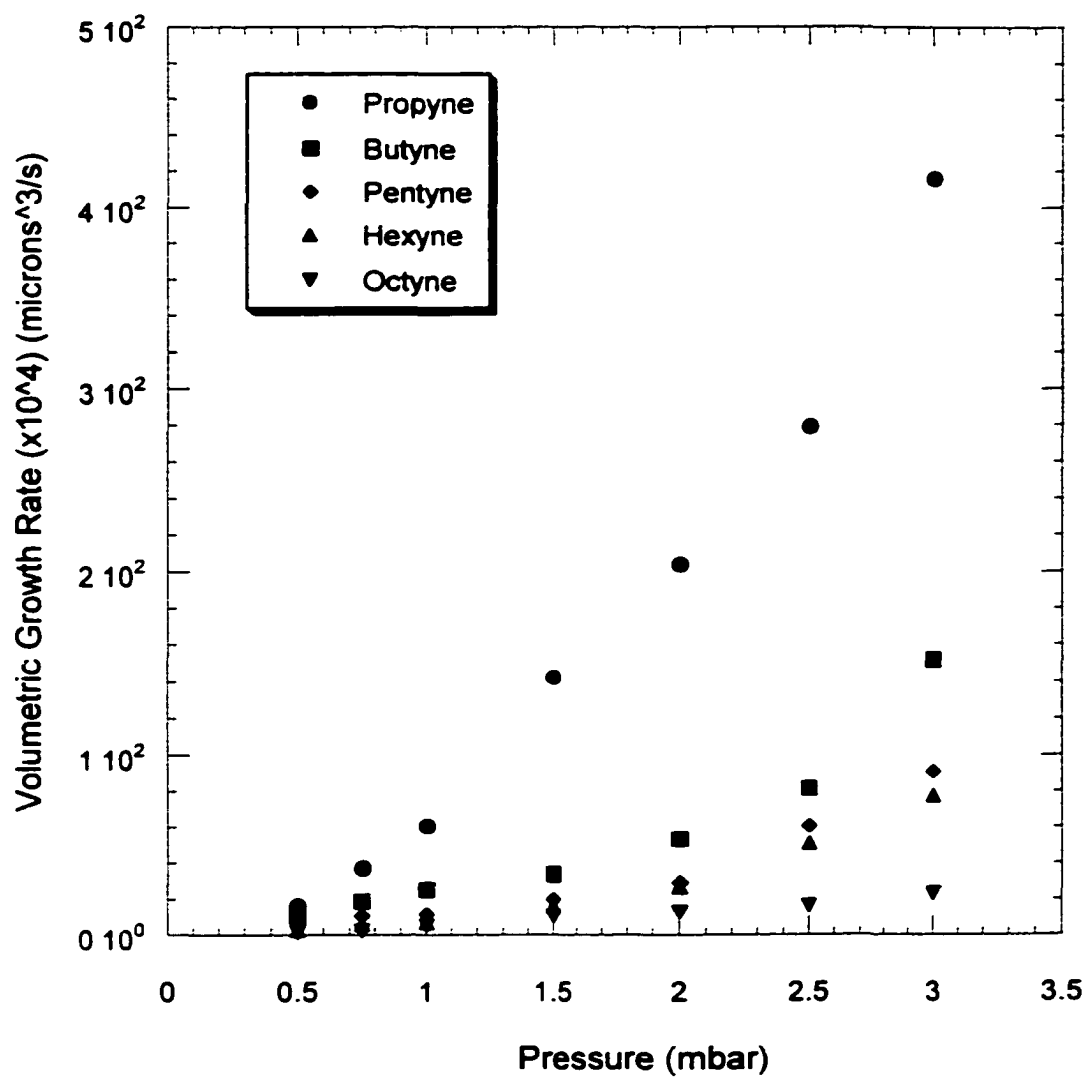


Figure 5.13 Volumetric growth rate as a function of partial pressure for alkynes-linear.

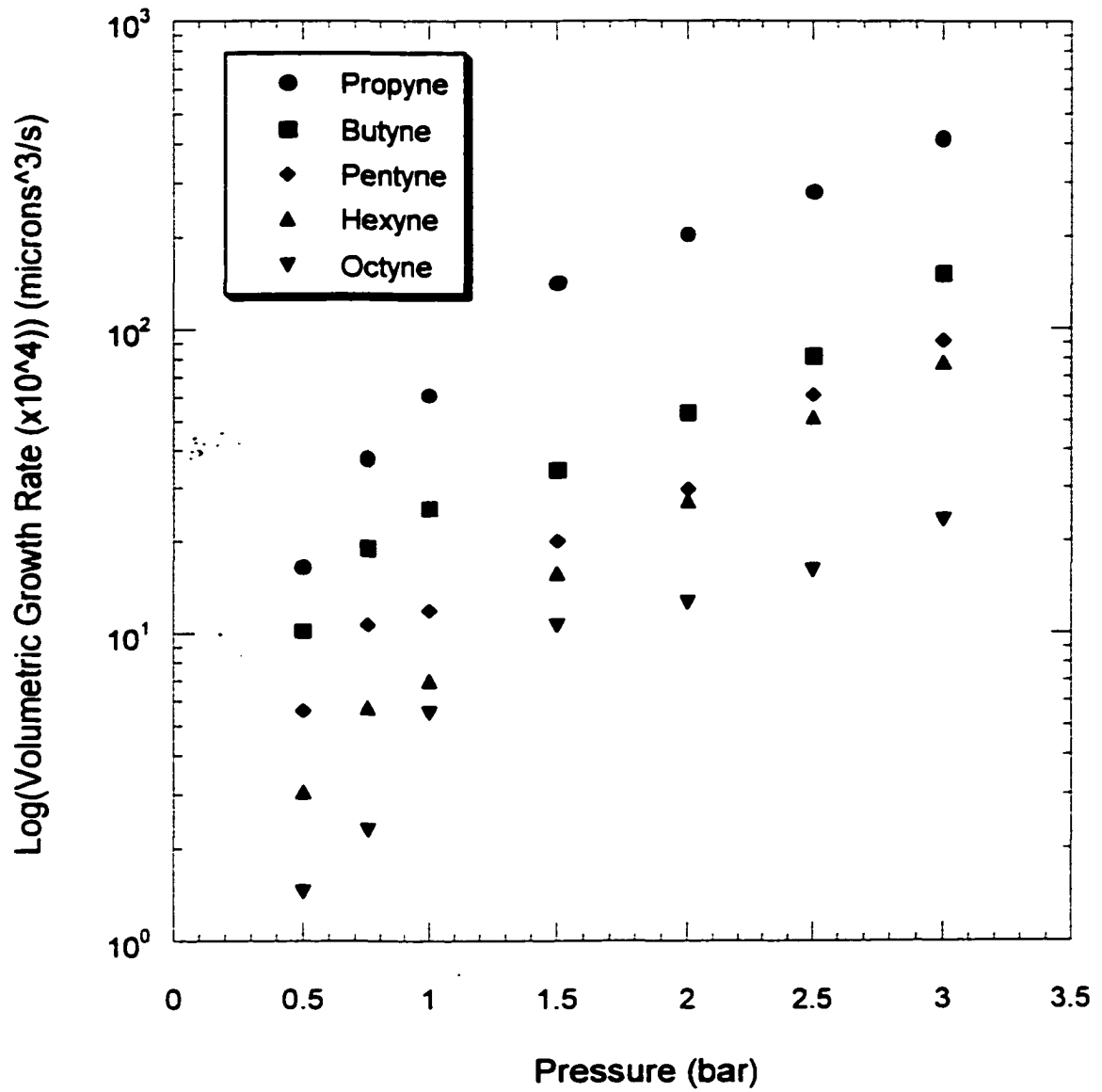
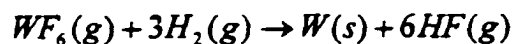


Figure 5.14 Volumetric growth rate as a function of partial pressure for alkynes-logarithm.

5.2 Deposition of Tungsten

The reaction utilized for deposition of the tungsten was hydrogen reduction of tungsten hexafluoride according to the following overall reaction:



A tungsten wire with a diameter of 300 μm was used as the substrate in all experiments. The reactor was loaded with a mixture of WF_6 (g) and H_2 (g) having a molar ratio of 1:1 at a total pressure of 1400 mbar. The laser power was also varied from 0.6 W to 2.6 W.

The resultant tungsten rod growth rates as a function of laser power is shown in Figure 5.15. From Figure 5.15, it can be seen that the growth rate increases linearly with the incident laser power, which is an indication of a mass transport limited process in this laser power region. The morphology and shape of tungsten rods are shown in Fig. 5.16. Generally, at low laser powers ($P < 1.3$ W), i.e. at low deposition temperatures, single crystal rods were obtained; at intermediate laser powers (1.3 W $< P < 2.5$ W) polycrystalline rods were produced; and at rods grown at laser powers above 2.5 W, lump-like, small-grained or large-grained rods result (see Figure 5.16).

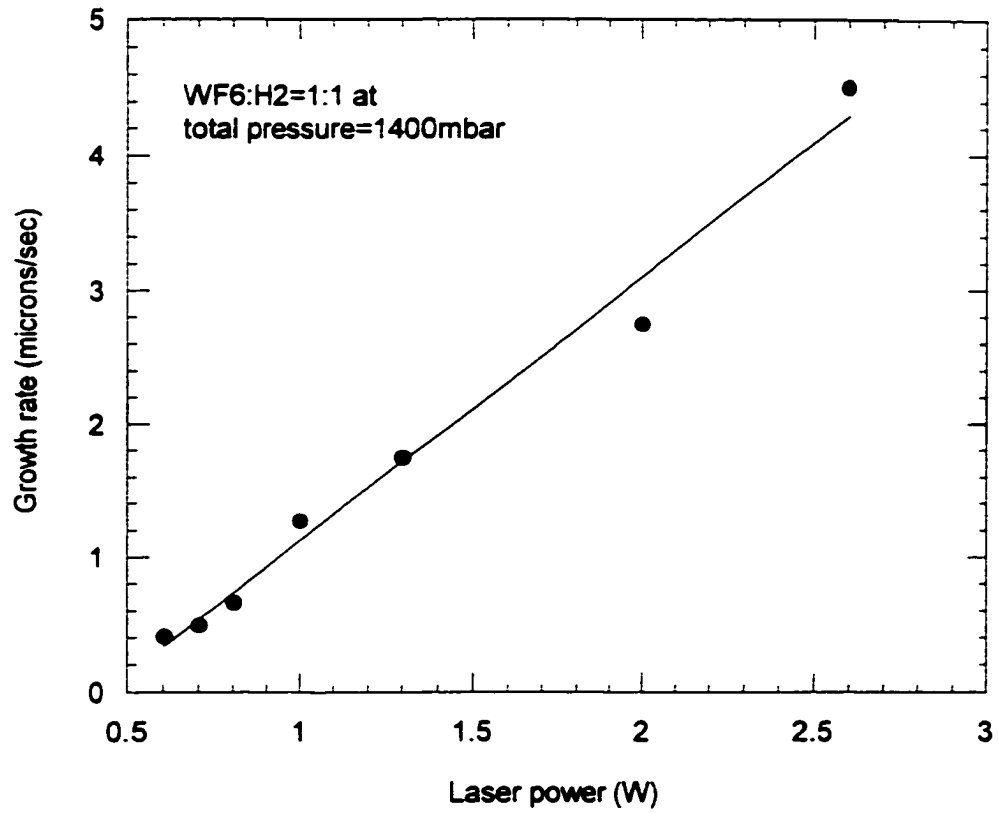


Figure 5.15 Growth rate as a function of laser power for tungsten deposition.

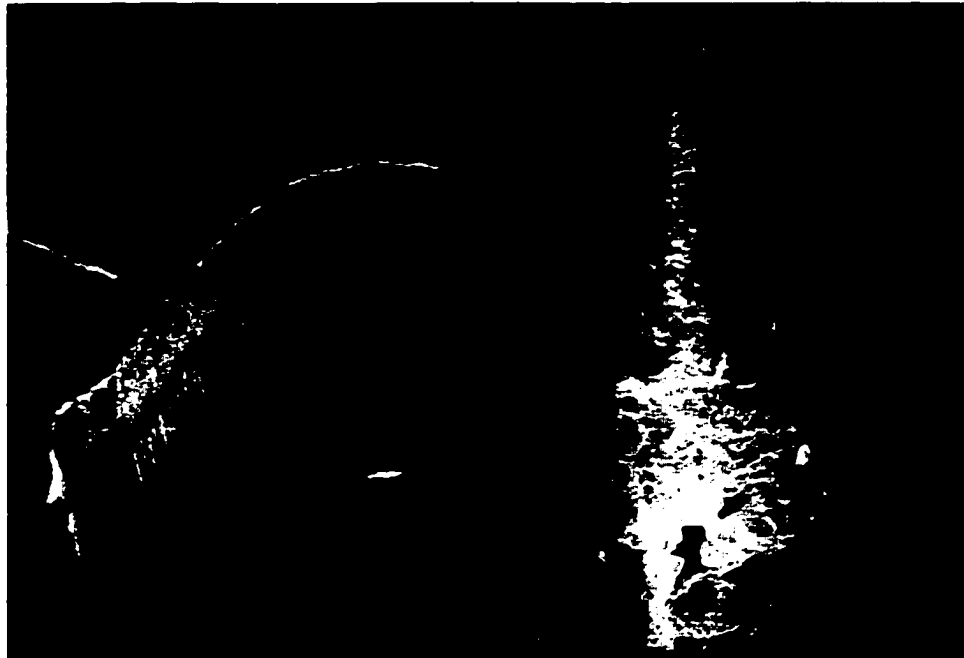


Figure 5.16 Rods in different morphologies.

The rod diameter as a function of laser power is plotted in Figure 5.17 from which it can be seen that the rod diameter depends linearly on the laser power. This dependence follows the same explanation as those for carbon deposition.

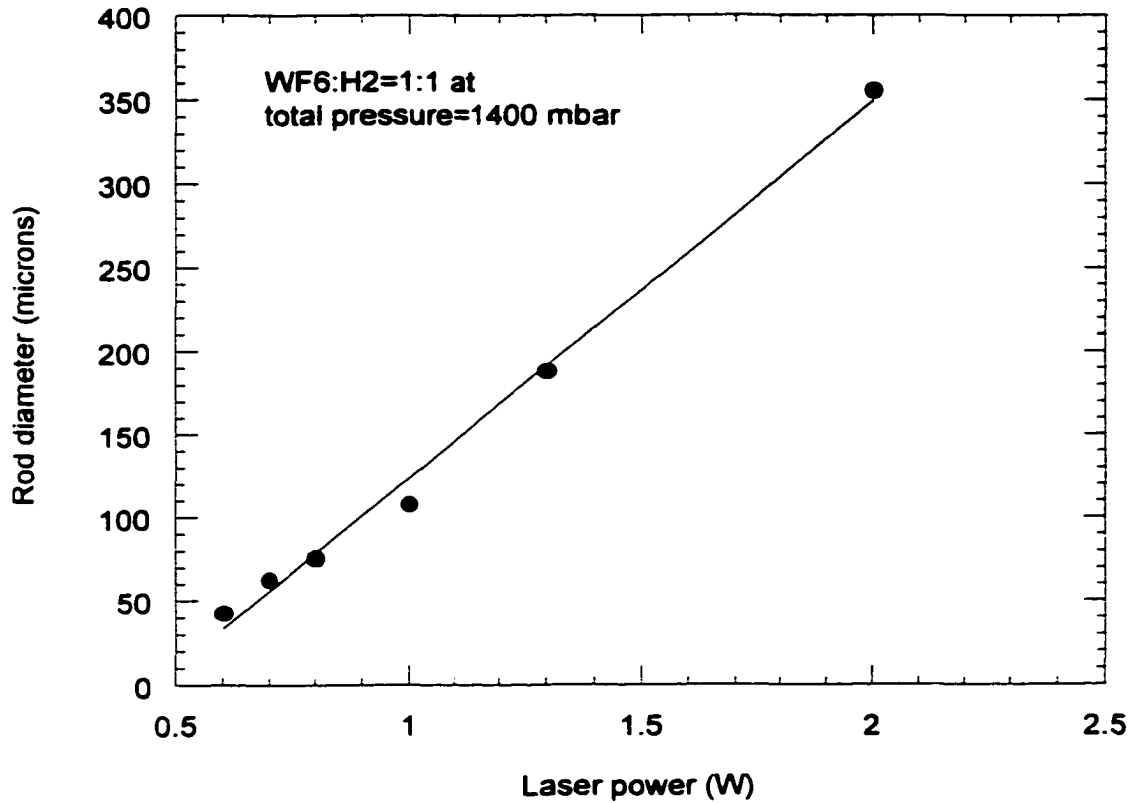
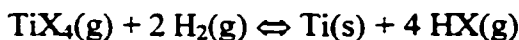


Figure 5.17 Rod diameter as a function of laser power for tungsten deposition.

5.3 Deposition of Titanium and Hafnium

Attempts to grow titanium and hafnium rods from TiI_4 and $HfCl_4$, respectively, failed. Titanium is difficult to deposit from the halides since the metal can not be reduced

by hydrogen at temperatures below the melting point of the metal, which means that the following reaction can not be utilized.



Here X = Cl, Br, I.

Use of a pyrolytic reaction like the one below is also not work either. The reason is probably because of the formation of stable TiX_3 and TiX_2 compounds.



Of all the titanium halides, TiI_4 is the most likely to work since it is the least stable halide. The major problem of using titanium tetraiodide is its low vapor pressure even at high temperatures (boiling point 377 °C). Other problems of using titanium tetraiodide include its highly corrosive properties, especially at elevated temperatures.

As mentioned earlier, titanium tetrachloride with a boiling point of 137 °C would give high precursor pressures in the existing equipment, but the stability of this precursor is too high. The only way to deposit titanium is probably to change the type of precursors and use organometallic titanium compounds instead. There exist a couple of organic titanium compounds that could be used in the existing LCVD system: bis(t-butylcyclopentadienyl) titanium trichloride, bis(cyclopentadienyl) titanium dichloride and dimethylbis(t-butylcyclopentadienyl) titanium. One possible problem using

organometallic titanium compounds is that they contain carbon. The carbon-involved deposition process means that TiC may form instead of Ti.

What have been said about titanium can also be said about hafnium. This means that the best solution is to switch to organometallic hafnium precursors in the future.

CHAPTER 6

CONCLUSIONS AND FUTURE WORK

In summary this work has shown that the different alkynes, i.e. propyne, butyne, pentyne, hexyne, and octyne, are attractive precursors for the growth of carbon microstructures and tungsten hexafluoride is an attractive precursor for the growth of tungsten microstructures using the 3D-LCVD process. Deposition rate in excess of 3 mm/s was obtained for LCVD of carbon using propyne as the precursor.

In order to examine the precursors above, a high-pressure laser chemical vapor deposition system was designed, built, and successfully used for laser assisted gas phase deposition of carbon and refractory metal microstructures. The system was designed to operate at very high precursor temperatures (up to 400 °C) so that a wide range of precursors could be evaporated or sublimated. The system was very flexible in a way that no change, or very little change, was needed when testing a different precursor. This system proved to be an effective and efficient tool in order to test new precursors.

The deposition rate of carbon as a function of laser power resulted in an exponential increase in growth rate for low laser powers (0.5 – 1 W). This laser power region was identified as the kinetically limited region. The growth rate increased linearly

when further increasing the laser power from 1 W to 1.5 W. The laser power region from 1 W to 1.5 W was identified as the mass transport limited region. The rod diameter increased linearly with increasing laser power for each alkyne at a constant pressure. The rod diameter decreased with increasing molecular weight. Both of two observations can be explained from different activation energies.

The deposition rate of carbon as a function partial pressure of the precursor increased as a power function (deposition rate^Y) where Y is 1.5 – 2.5 depending on the precursor. The precursor having the highest Y was propyne which increasing most dramatically as a function of partial pressure. A decreased reaction order with increasing molecular weight of alkynes was also observed. This behavior was not fully explained, but was probably the result of the complicated growth mechanisms involved in this type of gas phase processes.

The rod diameter as a function of partial pressure of the precursors followed a complicated pattern, which could not be explained without further experiments. In order to explain why the rod diameter from the 3 lightest alkynes first increases with increasing partial pressure and then decreases, density measurements of the carbon rods should be performed.

The volumetric growth rate as a function of partial pressures of the precursors was also plotted. Two linear regions were distinguished with a transition at about 1.25 W.

The morphology and the microstructure of the rods depended both on partial pressure of the precursor and laser power (temperature). As we move from a low temperature to a high temperature, the microstructure changes from amorphous to small-grained to large-grained (polycrystalline). The effect of pressure is as expected the

opposite, as we increase the pressure, the microstructure changed from polycrystalline to amorphous.

For tungsten deposition, the growth rate increases linearly with increasing laser power, which depicts a mass transport limited process. The rod diameter also increased linearly with increasing laser power, and which follows the same explanation as that of carbon deposition. For tungsten rod microstructure, at low laser power, single crystalline structure was obtained; at middle laser power, polycrystalline structure was produced; and at high laser power, lump-like structure was obtained. For future work, more experiments are scheduled for this project, such as varying the $WF_6:H_2$ molar ratio, investigating the effects of hydrogen on growth rate, and varying partial pressure but fixing the gas mixture ratio, investigating the partial pressure effects on growth rate. Visual and composition analysis of the tungsten rods could be performed with a scanning electron microscope (SEM) using secondary electron imaging (SEI) and energy dispersed X-ray spectroscopy (EDS). The microstructure could be investigated with a single crystal X-ray diffractometer.

Finally, for titanium and hafnium deposition, due to the very low vapor pressure of the currently-used precursors, which would need a sublimation temperature of 400 °C, new organic precursors of both titanium and hafnium should be chosen to test the compatibility with this system. Extensive experiments need to be done to investigate the mechanisms and key parameter effects on deposition.

REFERENCES

- [1] J. Maxwell, Ph.D Thesis, Renssaeler Polytechnic Institute, 1996.
- [2] J. Narayan, M.S. Thesis, Louisiana Tech University, 2000
- [3] S. Gnanavelu, M.S. Thesis, Louisiana Tech University, 2000
- [4] L. Beluze, A. Bertsch, P. Renaud, SPIE vol.3680, "Microstereolithography: a new process to build complex 3D objects", 808-817, 1999
- [5] X. Huang, R.O. Warrington, C.R. Friedrich, SPIE vol. 3511, "Microstructures fabricated by laser induced polymization", 50-55, 1998
- [6] P.M. Martin, D. W. Matson, W.D. Bennett, D.C. Stewart, Y. Lin, SPIE vol. 3680, "Laser Micromachined and Laminated Microfluidic Components for Miniatured Thermal, Chemical and Biological Systems", 826-833, 1999
- [7] P.V. Zant, Microchip Fabrication, Third Edition, 1997
- [8] M. Madou, Fundamentals of Microfabrication, 1997
- [9] P.B. Comita, Advanced Materials, vol. 2 n 2, "Surface Modification with Lasers", 82-90, 1990
- [10] G. Zong, Ph.D Thesis, University of Texas at Austin, 1992
- [11] J. Mazumder, A. Kar, "Theory and Application of Laser Chemical Vapor Deposition", Plenum Press, 1995
- [12] D. Bauerle, "Laser Processing and Chemistry", Springer-Verlag Berlin Heidelberg New York
- [13] M. Meunier, P. Desjardins, M. Tabbal, N. Elyaagoubi, R. Izquierdo, A. Yelon, "Laser Processing of Tungsten from WF_6 and SiH_4 ", Applied Surface Science, vol. 86, 475-483, 1995

- [14] S. Kimura, J. Tanaka, H. Noda, T. Toyabe, S. Ihara, "Short-Channel-Effect-Suppressed Sub-0.1- μm Grooved-Gate MOSFET's with W Gate", *IEEE Transactions on Electron Devices*, vol. 42, No. 1, 94-99, January, 1995
- [15] P. Kubat, P. Engst, "Study of The Formation of Titanium Deposit in The Excimer Laser Decomposition of Titanium Tetrachloride Time Resolved UV Spectroscopy", *Applied Surface Science*, vol. 64, 97-101, 1993
- [16] W.J. Lackey, J.A. Hanigofsky, G.B. Freeman, "Experimental Whisker Growth and Thermodynamic Study of the Hafnium Carbide System for Chemical Vapor Deposition Application", *J. Am. Ceram. Soc.* Vol. 73, No. 6, 1593-98, 1990
- [17] R. Putzar, H.C. Petzold, U. Weigmann, "Laser-induced Metal Deposition: a Tool for the Repair of Clear Defects on X-ray Masks", *Chemtronics*, vol. 4, 172-179, Sept. 1989
- [18] G. Auvert, "Laser Chemical Vapor Deposition for Microelectronics", *Applied Surface Science*. vol. 86, 466-474, 1995
- [19] M. Meunier, R. Izquierdo, P. Desjardins, M. Tabbal, A. Yelon, "Laser Direct Writing of Tungsten from WF_6 ", *Thin Solid Films*, vol. 218, 137-143, 1992
- [20] G. Reisse, F. Gansicke, R. Ebert, U. Illmann, H. Johansen, "Laser-induced Chemical Vapor Deposition of Conductive and Insulating Thin Film", *Applied Surface Science*, vol. 54, 84-88, 1992
- [21] L. Xuebiao, Z. Jie, Q. Mingxin, "Laser-induced Thermochemical Vapor Deposition of Tungsten Films and Its Application", *Thin Solid Film*, vol. 196, 95-101, 1991
- [22] R. Kullmer, P. Kargl, D. Bauerle, "Laser-induced Deposition of Tungsten from Tungsten Hexachloride", *Thin Solid Film*, vol. 218, 122-136, 1992
- [23] M. Meunier, C. Lavoie, S. Boivin, R. Izquierdo, P. Desjardins, "Modeling KrF Excimer Laser Induced Deposition of Titanium from Titanium Tetrachloride", *Applied Surface Science*, vol. 54, 52-55, 1992
- [24] W.B. Chou, M.N. Azer, J. Mazumder, "Laser Chemical Vapor Deposition of Ti from TiBr_4 ", *J. Appl. Phys.*, vol. 66, 191-195, Jul. 1998
- [25] H.O. Pierson, "Handbook of Chemical Vapor Deposition-Principles, Technology, and Applications", Noyes Publications, 165-170, 1992
- [26] H. Westberg, M. Boman, A.S. Norekrans, J.-O. Carlsson, "Carbon Growth by Thermal Laser-assisted Chemical Vapor Deposition", *Thin Solid Film*, vol. 215, 126-133, 1992

- [27] J. L. Maxwell, J. Pegna, E. Hill, "Gas-Phase Laser-Induced Pyrolysis of Tapered Microstructures", Proc. Solid Freeform Fabrication Symposium, 143-150, 1995
- [28] K. Petersen, "Silicon as a Mechanical Material", Proc. of IEEE, vol. 70, No. 5, 39-77, May 1982
- [29] M. Hakim, "Chemical Vapor Deposition of Hafnium Nitride and Hafnium Carbide on Tungsten Wires", Proc. 5th Int. Conf. On CVD, 634-649.
- [30] W. Lackey, J. Hanigofsky, G. Freeman, "Experimental Whisker Growth and Thermodynamic Study of the Hafnium Carbide System for Chemical Vapor Deposition Application", J. Amer. Ceram. Soc., vol. 73, No.6, 1593-98, 1990
- [31] M. Futamoto, I. Yuito, U. Kawabe, "Hafnium Carbide and Nitride Whisker Growth by Chemical Vapor Deposition", J. Cryst. Growth, vol. 61 No. 1, 69-74, 1983
- [32] D. Bauerle, "Laser-Induced Chemical Vapor Deposition", Springer Series in Chemical Physics 39, Laser Proceeding and Diagnostics, 166-182, 1984
- [33] F.T. Wallenberger, P.C. Nordine, "Strong, Pure, and Uniform Carbon Fibers Obtained Directly from the Vapor Phase", Science, Vol. 260, 66-68, April, 1993
- [34] J. Maxwell, J. Pegna, D.A. Deangelis, D.V. Messia, "Three-Dimensional Laser Chemical Vapor Deposition of Nickel-Iron Alloys", Mat. Res. Soc. Symp. Proc., Vol. 397, 601-606, 1996
- [35] J. Pegna, D. Messia, W.H. Lee, "Trussed Structures: Freeform Fabrication without the Layers", Proc. Solid Freeform Fabrication Symposium, Austin, Texas, August, 1997
- [36] D. Messia, J. Pegna, W.H. Lee, "Layered Micro-Wall Structures from the Gas Phase", Proc. Solid Freeform Fabrication Symposium, Austin, Texas, August, 1997
- [37] K. Williams, J. Maxwell, K. Larsson, M. Boman, "Freeform Fabrication of Functional Microsolenoids, Electromagnets and Helical Springs Using High-Pressure Laser Chemical Vapor Deposition", IEEE, 232-237, 1999
- [38] S.D. Allen, A.B. Tringubo, "Laser Chemical Vapor Deposition of Selected Area Fe and W Film", J. Appl. Phys. Vol. 54, No. 3, 1641-1643, March, 1989